Aalto University
School of Science and Technology
Faculty of Information and Natural Sciences

Petri Heikkinen

NMR Techniques at Liquid Helium Temperatures

Master's thesis submitted in partial fulfillment of the requirements for the degree of Master of Science in Technology in the Degree Programme in Engineering Physics.

Espoo, June 13, 2010

Supervisor: Professor Matti Kaivola
Instructor: Professor Matti Krusius

AALTO UNIVERSITY
SCHOOL OF SCIENCE AND TECHNOLOGY
FACULTY OF INFORMATION AND NATURAL SCIENCES

ABSTRACT OF THE
MASTER'S THESIS

Author:	Petri Heikkinen
Title:	NMR Techniques at Liquid Helium Temperatures
Title in Finnish:	Ydinmagneettinen resonanssimittaus nestemäisen heliumin lämpötiloissa
Degree Programme:	Degree Programme in Engineering Physics
Major subject:	Materials Physics
Minor subject:	Microelectronics (Semiconductor Technology)
Chair:	Tfy-44 Materials Physics
Supervisor:	Prof. Matti Kaivola
Instructor:	Prof. Matti Krusius

Abstract:

In this master's thesis I describe our recently upgraded measurement techniques and devices based on the nuclear magnetic resonance (NMR) techniques used to investigate superfluid helium. At present, our research concentrates on the superfluid phase ^{3}He-B. The most important part in our NMR circuit is a two-stage cryogenic MESFET preamplifier operating at 4 K. It is capacitively coupled to a high-Q ($Q \approx 40000$ in test conditions) LC-resonance circuit. The ^{3}He-B sample is placed inside the superconducting pick-up coil, which is a part of the resonance circuit. High sensitivity and low noise levels are the requirements for the measurement circuitry. Our measurements have shown the signal-to-noise level to be around 8000 which is enough to detect small changes in the signal from the superfluid ^{3}He-B sample. I also present the theories on which our measurements are based and analyze the NMR responses measured from the normal fluid and from the superfluid. The effect of rotation and vortices on the signal response is explained. We have also measured spin-wave spectra at different temperatures and rotation speeds. The data we have gathered shows the NMR response to be congruent with the theories and earlier measurements. All ^{3}He measurements have been performed in a rotating cryostat, with which we can achieve sample temperatures below 500 μK. Overall, the measurement accuracy is enough to investigate the properties of ^{3}He-B on approaching the zero temperature limit.

Date: June 13, 2010	Language: English
Number of pages: 73	Keywords: NMR, superfluid, helium-3

AALTO-YLIOPISTO
TEKNILLINEN KORKEAKOULU
INFORMAATIO- JA LUONNONTIETEIDEN TIEDEKUNTA

DIPLOMITYÖN TIIVISTELMÄ

Tekijä:	Petri Heikkinen
Työn nimi:	Ydinmagneettinen resonanssimittaus nestemäisen heliumin lämpötiloissa
English title:	NMR Techniques at Liquid Helium Temperatures
Koulutusohjelma:	Teknillisen fysiikan koulutusohjelma
Pääaine:	Materiaalifysiikka
Sivuaine:	Mikroelektroniikka (puolijohdeteknologia)
Professuurin koodi ja nimi:	Tfy-44 Materiaalifysiikka
Työn valvoja:	Prof. Matti Kaivola
Työn ohjaaja:	Prof. Matti Krusius

Tiivistelmä:

Tässä diplomityössä esittelen supranesteheliumin tutkimuksessa käyttämiämme ja viimeisen vuoden aikana uudistamiamme ydinmagneettiseen resonanssiin (nuclear magnetic resonance, NMR) perustuvia mittaustekniikoita. Tällä hetkellä tutkimuksemme keskittyvät ^{3}He-B supranesteeseen. NMR-mittauspiirimme tärkein osa on 4 K:n lämpötilassa toimiva kahden MESFET:in kaskodikytkentään perustuva esivahvistin, joka on kapasitiivisesti kytketty korkean Q-arvon (testiolosuhteissamme $Q \approx 40000$) LC-resonanssipiiriin. ^{3}He-B supranestenäyte on sijoitettu resonanssipiirin osana olevan suprajohtavan kelan sisään. Mittauspiiriltä vaaditaan korkeaa herkkyyttä ja vähäistä kohinatasoa. Olemme mitanneet signaali-kohinasuhteen olevan luokkaa 8000, joka on riittävän hyvä havaitaksemme pienet näytteen aiheuttamat muutokset signaalissa. Esittelen myös mittaustemme perustana olevan teorian ja analysoin sekä normaali- että supranestetilasta mittaamiamme NMR-vasteita. Myös pyörityksen ja kvantittuneiden virtauspyörteiden eli vorteksien vaikutus NMR-signaaliin selostetaan. Olemme mitanneet spin-aaltospektrejä eri lämpötiloissa sekä eri pyöritysnopeuksilla. Keräämämme mittausaineisto osoittaa NMR-vasteen olevan teorioiden mukainen. Kaikki ^{3}He-mittaukset on tehty pyörivässä kryostaatissa, jolla voimme jäähdyttää näytteemme alle 500 μK:n lämpötilaan. Kaiken kaikkiaan laitteistomme pystyy riittävän tarkkoihin NMR-mittauksiin tutkiessamme ^{3}He-B:n ominaisuuksia nollalämpötilarajaa lähestyttäessä.

Päivämäärä: 13.6.2010	Kieli: Englanti
Sivumäärä: 73	Avainsanat: ydinmagneettinen resonanssi, supraneste, helium-3

Acknowledgements

This Master's thesis was done in ROTA group in the Low Temperature Laboratory in Aalto University School of Science and Technology during years 2009 and 2010.

I wish to thank professor Matti Kaivola for supervising this thesis. I am also very thankful for my instructor and our group leader, professor Matti Krusius, and the other members of the ROTA-group, Vladimir Eltsov, Rob de Graaf, and Jaakko Hosio, for their valuable comments, advice, and corrections during the practical part and the writing of this Master's thesis. Without them the result would not be even close to the quality it is now. David Schmoranzer from Charles University gets my thanks for making lots of testing of the devices. I thank the guys in the workshop, Arvi Isomäki, Markku Korhonen, and Hannu Kaukelin, for making my drawings to live and for giving me some important lessons on what really is practically possible and what is not. I am also grateful to the administrative staff of the laboratory for their help in the practical matters. I want to express my special gratitude to the laboratory's director, professor Mikko Paalanen, for giving me the possibility to work in the Low Temperature Lab back in 2005.

I wish to thank my parents Päivi and Markku for their continuous help and support, which surely encouraged me to start studying physics in the first place.

Finally, huge thanks to all the great people I have got to know during my student days in Otaniemi, mostly through the activities in the Guild of Physics and in the late Student Union of Helsinki University of Technology: Pacman, Raati06, Teekkarijaosto07, and all the others, how could I thank you enough for making the past seven years definitely the most memorable and the funniest years of my life. So far, because the path is just beginning and the show must go on!

Espoo, June 13, 2010

Petri Heikkinen

Contents

Chapter 1

Introduction

Helium is the second lightest and the second most common element in the universe after hydrogen. It has two stable isotopes, namely ^{3}He and ^{4}He, of which ^{4}He is far more abundant: in the atmosphere ^{3}He constitutes a fraction $1.3 \cdot 10^{-6}$ of helium gas [1]. Obtaining ^{3}He in a reasonable amount by separating it from ^{4}He is very costly. Also mining for it is useless since in the Earth's regolith no commercial concentrations are present because the ozone layer filters out the most of the cosmic radiation coming from the sun and containing ^{3}He. So it has been proposed that ^{3}He could be mined from the Moon's regolith where it has been captured from the solar wind over billions of years, and its concentration in the regolith is now on the order of 0.01 ppm [2, 3]. Insufficiency of natural sources of ^{3}He results in most of the ^{3}He in use today being a byproduct of tritium which is manufactured in nuclear reactors through neutron bombardment of lithium. At present, the price of ^{3}He is high, of the order of thousands of €/l of gas at NTP.

The boiling point of liquid helium is rather low (4.2 K for ^{4}He and 3.2 K for ^{3}He at atmospheric pressure). Helium also has the unique property of remaining in the liquid state down to absolute zero. It can be solidified only by applying high pressures. The reasons for this are the low atomic mass giving rise to a large zero-point energy and the weak interaction between the atoms [1]. But what makes helium even more interesting is the fact that at low temperatures both stable isotopes undergo a transition to superfluid states (2.2 K for ^{4}He and 1.1 mK for ^{3}He at atmospheric pressure). Superfluidity and superconductivity are related phenomena: in a superconductor the electron flow transports current without resistance, and in a superfluid entire atoms condense to the superfluid state and move without friction, i.e., the superfluid condensate flows without viscosity.

There is a fundamental quantum mechanical difference between the two helium isotopes: the ^{4}He atom is a boson and the ^{3}He atom a fermion with spin $1/2$. In liquid ^{4}He the superfluidity arises when a macroscopic fraction of atoms occupies the minimum energy state in a process related to Bose-Einstein condensation.

^{3}He atoms obey the Pauli exclusion principle which states that no two identical fermions may occupy the same quantum state, so liquid ^{3}He becomes superfluid through Cooper pairing similarly to electrons in superconductors.

When a superfluid is rotated, quantized vortices are spontaneously formed. In the simplest case, as is the case of superfluid ^{4}He, the vortices are axially symmetric vortices with a singular hard core where a trapped persistent superfluid current flows around "holes" in which the amplitude of the superfluid order parameter vanishes. As a reasonable approximation, this type of vortex can be regarded as a cylindrical tube with a core filled with normal liquid. In the case of superfluid ^{3}He the situation is different. In rotation there exist nonsingular hard core vortices, continuous core vortices, and composite core vortices. The presence of each type of vortex depends on temperature, pressure, and magnetic field applied to the sample [4].

In the Low Temperature Laboratory of the Aalto University School of Science and Technology the vortices in superfluid ^{3}He have been studied in a specially designed and constructed rotating cryostat since the beginning of the 80's [5, 6]. Already soon after the first rotating experiments in late 1982 the first vortex structures were identified [7, 8].

Nuclear magnetic resonance (NMR) techniques have proven to be the best method to study the properties of vortices in rotating superfluid ^{3}He. The measurements at very low temperatures demand high sensitivity and low noise, even if the NMR signal itself is not very small, but since changes in the signal are extremely small at the lowest temperatures. Therefore, a cooled preamplifier has been placed inside the cryostat. When this was done for the first time [9, 10] the sensitivity in the vortex measurements was improved so much that it became possible to see the formation of vortices one-by-one [11–13].

This thesis describes the present instrumentation, mainly the cryogenic GaAs MESFET preamplifier and the high-Q LC resonance circuit, used for amplifying the NMR signals, and compares new results with the ones achieved with the previous design. Also the differences between the current and the past designs are reported.

Chapter 2

Theory of NMR-measurements in ^{3}He-B

2.1 Basic properties of superfluid ^{3}He and its vortices

^{3}He undergoes a superfluid transition at a pressure-dependent critical temperature T_c. The weakness of the Cooper pairing interaction makes the condensation energy very small, so the superfluidity in ^{3}He is only observed at millikelvin temperatures. The Cooper pairs are in the same two-particle state, having a nonzero spin $S = 1$ and a relative orbital angular momentum $L = 1$ [14, 15]. The superfluid phase can be described by an order parameter that reflects the broken symmetries associated with the phase transition. For superfluid ^{3}He the Cooper pair state is determined by nine complex amplitudes, corresponding to the three possible projections of both S_z and L_z, and the order parameter is usually represented by a complex 3×3 matrix $A_{\mu j}$, where the index μ refers to spin and the index j to orbital degrees of freedom. Because of the complicated order parameter structure, superfluid ^{3}He exhibits magnetic and liquid-crystal-like behavior, supports many kinds of topological defects, including a variety of vortices, and can exist in several superfluid phases with different symmetry properties [16–19]. In the case of superfluid ^{4}He the order parameter has the simpler form of a scalar wave function $\psi = |\psi| e^{i\phi}$ [20].

Fig. 2.1 shows the phase diagram of ^{3}He at low temperatures at zero magnetic field as a function of temperature and pressure. The ^{3}He-A phase corresponds to the Anderson-Brinkman-Morel (ABM) state [21] and the dominant phase at low magnetic field, the ^{3}He-B phase, corresponds to the Balian-Werthamer (BW) state [22]. In this thesis we concentrate mainly on superfluid ^{3}He-B, in addition to some measurements in the normal liquid ^{3}He which obeys the Fermi liquid

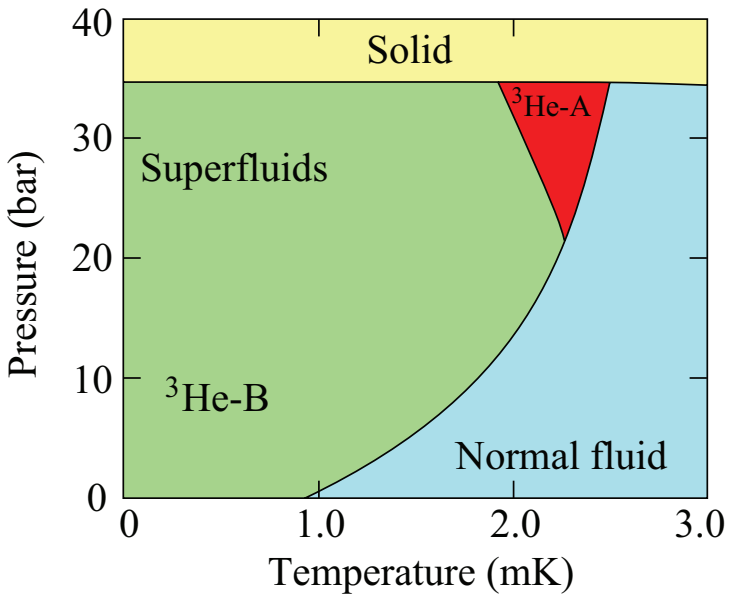

Figure 2.1: *Phase diagram of liquid ^{3}He at zero magnetic field. The external magnetic field makes the A phase more favorable moving the AB transition towards lower temperatures.*

theory [23]. For ^{3}He-B the order parameter has the form

$$A_{\mu j} = \Delta e^{i\phi} \mathbf{R}_{\mu j}(\hat{\mathbf{n}}, \theta), \tag{2.1}$$

where Δ is superfluid energy gap, ϕ is an overall phase factor, $\mathbf{R}(\hat{\mathbf{n}}, \theta)$ is a rotation matrix describing the relative orientation of the spin and orbital spaces, $\hat{\mathbf{n}}$ is the unit vector in the direction of the axis around which the spin and orbital coordinate axes have been rotated with respect to each other, and θ is the angle of this rotation [24].

2.1.1 Vortices in ^{3}He-B

When a superfluid is rotated, quantized vortices are created. To understand various properties of superfluids, the study of vortices is of crucial importance. The phenomenological two-fluid model comes handy in explaining the phenomena. The superfluid can be regarded as a mixture of two liquids, one part is a normal viscous liquid with density ρ_n and velocity $\mathbf{v}_n$, and the other part is superfluid, with density $\rho_s = \rho - \rho_n$ and velocity $\mathbf{v}_s$. The total density is marked as ρ. The behavior of the superfluid component is described by the order parameter. Projecting the quantum mechanical momentum operator on the order parameter gives

(let us deal here with the order parameter of ^{4}He because the discussion applies to ^{3}He-B with only a few modifications)

$$\hat{\mathbf{p}}\psi = -i\hbar\nabla\psi = \hbar(\nabla\phi)\psi = \mathbf{p}\psi. \tag{2.2}$$

So the linear momentum has the form $\mathbf{p} = \hbar\nabla\phi$. The superfluid momentum can also be written by using the superfluid velocity $\mathbf{v}_s$ and the mass of the ^{4}He atom, $\mathbf{p} = m_4\mathbf{v}_s$. Combining these we get the superfluid velocity of ^{4}He as determined by the spatial gradient of the phase,

$$\mathbf{v}_s = \frac{\hbar}{m_4}\nabla\phi. \tag{2.3}$$

By taking the curl of $\mathbf{v}_s$, we get

$$\nabla \times \mathbf{v}_s = \nabla \times \frac{\hbar}{m_4}\nabla\phi = 0. \tag{2.4}$$

This implies that the superfluid as such is irrotational. However, this does not rule out the possibility of the rotational motion around a region where the order parameter vanishes (for example around normal liquid). One round around this kind of region must leave the order parameter ψ unchanged, i.e., ϕ can change only by multiples of 2π. Thus we get the circulation κ,

$$\kappa = \oint \mathbf{v}_s \cdot d\mathbf{r} = \frac{\hbar}{m_4}\oint \nabla\phi \cdot d\mathbf{r} = \frac{\hbar}{m_4}(2\pi n) = n\frac{h}{m_4}, \tag{2.5}$$

where n is an integer. We see that the circulation in superfluid ^{4}He is quantized in integral multiples of $\frac{h}{m_4}(= 0.0998\frac{\mathrm{mm}^2}{\mathrm{s}})$. This explains the rotation of the superfluid: the superfluid mimics solid-body rotation because of the presence of singular regions inside which the order parameter vanishes and around which the superfluid rotates. These regions are called the cores of the vortex lines. Each quantized vortex line carries one quantum of circulation in equilibrium situations, i. e., it is energetically more favourable to form n vortices with single quantum of circulation than one vortex with n quantums of circulation. In superfluid ^{4}He the vortex core has a diameter comparable to the coherence length $\xi \sim 0.1\,\mathrm{nm}$ [25]. A vortex line is a topologically stable object, so it cannot end in the middle of the condensate, but it either forms a continuous ring or ends at a wall.

^{3}He-B is an isotropic superfluid with a similar phase factor in the order parameter as the superfluid ^{4}He (Eq. (2.1)), so the above discussion can be applied to it as well. In ^{3}He-B the condensate is formed by pairs of atoms and the superfluid velocity is given by

$$\mathbf{v}_s = \frac{\hbar}{2m_3}\nabla\phi. \tag{2.6}$$

The quantum of circulation is $\frac{h}{2m_3}(= 0.066\frac{\mathrm{mm}^2}{\mathrm{s}})$. Due to the additional degrees of freedom, the vortices in ^{3}He-B have a superfluid hard core where the order parameter deviates strongly from the bulk. The core radius is of the order of the coherence length, $\xi(p,T) \gtrsim 10\,\mathrm{nm}$. Three different types of vortices have been observed experimentally in ^{3}He-B: the axisymmetric, the non-axisymmetric and the spin mass vortex [26, 27].

The presence of vortices in the rotating sample affects the counterflow $\mathbf{v} = \mathbf{v}_n - \mathbf{v}_s$. In the rotating cylindrical container filled with superfluid (like our sample cell) the velocity of the normal component in the laboratory frame is $\mathbf{v}_n = \overrightarrow{\Omega} \times \mathbf{r}$, where $\overrightarrow{\Omega}$ is the angular rotation velocity of the container. In the vortex-free state the superfluid velocity $\mathbf{v}_s = 0$. The minimum energy state corresponding to each rotation velocity is an Ω-dependent equilibrium density of rectilinear vortices in the sample. However, it is possible to maintain metastable vortex free flow up to certain level since there is an energy barrier preventing the vortex formation. This limiting Ω depends, e.g., on the temperature, the size of the sample, and the roughness of the walls of the container. When vortex lines appear in the sample, they form a bundle in the center of the container. Within this bundle the superfluid component mimics solid body rotation and the counterflow velocity is zero. Outside the bundle, in the vortex-free annulus, $v(r) = \Omega r - \Omega_v R^2/r$, where $\Omega_v = \Omega\frac{N}{N_0}$, R is the radius of the sample cylinder, N is the number of vortices in the bundle, and N_0 is the vortex number for the container with the equilibrium number of vortices at the rotation velocity Ω. Finally, when the minimum energy state is achieved, i.e., the sample has the equilibrium number of vortices and only a small vortex-free annulus next to the cylindrical wall, the counterflow velocity in the sample equals zero on average.

2.2 Basics of NMR

2.2.1 Introduction

Nuclear magnetic resonance provides a powerful way to examine atoms and their interactions. It can be used to probe atoms which have unpaired protons or neutrons in their nuclei, i.e., which have a nuclear spin. Important NMR isotopes are ^{1}H, ^{3}He, ^{13}C and ^{31}P. The atoms are immersed in a static polarizing magnetic field and are exposed to a second transverse oscillating excitation magnetic field. The absorption of the oscillating field in the sample is measured.

The total spin of protons and neutrons determines the NMR response of a nucleus. According to a simple shell model, with even number of both protons and neutrons the spin of a nucleus is zero, while with odd number of protons or neutrons (or both) the spin is the sum of the spins of the unpaired nucleons. When a

nucleus with unpaired nucleons, i.e., with a net spin, is placed in an external magnetic field H, the spin vector of the nucleus aligns itself with the field. A nucleus with spin I has $2I+1$ possible energy states. In the simplest case, where $I = 1/2$, there are two possible energy states determined by how the spin vector is aligned in the field. It is pointing either in the same direction or in the opposite direction in relation to the field direction. These two configurations are the low energy state and the high energy state. A transition between the two states is possible by the absorption or emission of a photon. A nucleus in the low energy state can absorb a photon and change the direction of its spin vector ending up in the high energy state. The opposite happens when a particle in the high energy state emits a photon. With higher values of I the number of possible states is higher increasing the number of possible transitions. This is seen as a peak broadening or as multiple absorption peaks in the measured NMR spectra. In addition, the electrons around the nucleus, interacting both with the nucleus and with the external field H, induces a chemical shift to the transition energies causing absorption frequency to shift. In molecules like ethyl alcohol, CH_3CH_2OH, the chemical shift is seen as three distinct hydrogen absorption peaks whose intensities are in the ratios 3:2:1 [28].

The energy of the transition photon must exactly match the energy difference between the two states. The energy of a photon, E, is related to its frequency, ω, through the equation

$$E = \hbar\omega. \tag{2.7}$$

The absorption frequency depends on the gyromagnetic ratio, γ, of the nucleus and on the intensity of the static magnetic field, H:

$$\omega_L = \gamma H. \tag{2.8}$$

In NMR, the absorption frequency (resonance frequency) is called the Larmor frequency and denoted as ω_L. The photons to be absorbed are provided by the transverse, oscillating field H_1, which can also be denoted the RF field H_{rf} since ω_L usually is in the radio frequency (RF) range. The signal in the NMR experiments results from the difference between the energy absorbed and the energy emitted by the atoms and is therefore proportional to the population difference between the states. The equilibrium population difference depends on the temperature T according to the Boltzmann statistics:

$$\frac{N^-}{N^+} = e^{-\Delta E/k_B T}, \tag{2.9}$$

where N^- and N^+ are the number of atoms in the high energy state and in the low energy state, respectively, and k_B is Boltzmann's constant. ΔE is the energy difference between these Zeeman states and thus depends on H. As the temperature

decreases, the amount of atoms in the low energy state increases, and vice versa. With NMR, very small population differences can be detected, making it a very sensitive tool for spectroscopy.

Continuous wave NMR (cw-NMR) is the simplest NMR method, and also the one we use in our measurements. It can be performed in two ways. In the first method, the RF field is continuously oscillating at a constant frequency ω and probing the energy levels of the sample while the static magnetic field is varied. In the second method, the frequency of the RF field is varied while H is kept constant. In both cases, the resulting signal is the same absorption signal, but in the first case it is measured as a function of H, and in the second case as a function of ω. The transformation between these two variables in ^{3}He-B measurements is presented in Sec. 2.3.4.

2.2.2 Relaxation processes

The material response to an applied magnetic field H is determined by the pressure and temperature dependent static magnetic susceptibility $\chi_0(p,T)$. The relationship between the equilibrium magnetization of the material, M_0, and the strength of the applied external field, H, is defined as

$$M_0 = \chi_0 H. \tag{2.10}$$

We can also write $M_z = \frac{\gamma\hbar n}{2}$, where $n = N^+ - N^-$ [28] and $+z$ is the direction of the static magnetic field H. In thermal equilibrium $M_0 = M_z$ and M_0 points in the $+z$ direction since $N^+ > N^-$, and there is no stable transverse magnetization ($< M_x >=< M_y >= 0$).

The net magnetization changes when the transverse oscillating RF field induces transitions in the spin system. If enough energy is put into the system, i.e., the amplitude of the RF field is high enough, it is possible to saturate the spin system and make $M_z = 0$. After the transverse excitation field is turned down, M_z relaxes to its equilibrium value according to the equation [29]

$$M_z = M_0(1 - e^{-t/T_1}), \tag{2.11}$$

where T_1 is the time constant called the longitudinal or spin-lattice relaxation time.

The oscillating transverse magnetic field H_{rf} also creates the transverse magnetization M_{xy} which rotates around the z axis at the Larmor frequency ω_L. The transverse net magnetization starts to dephase because each of the spins experiences a slightly different magnetic field and rotates at its own frequency. This is both due to the combination of molecular interactions and to local variations in H. Dephasing causes M_{xy} to return towards its equilibrium value, $M_{xy} = 0$. The

longer the elapsed time, the greater the phase difference and the smaller M_{xy}. The transverse magnetization relaxes according to the equation [29]

$$M_{xy} = M_{xy_0} e^{-t/T_2}, \tag{2.12}$$

where T_2 is the time constant called the transverse or spin-spin relaxation time. The T_1 and T_2 relaxation processes occur simultaneously usually with the restriction that T_2 is less than or equal to T_1: the transverse component M_{xy} rotates around the z axis dephasing and relaxing towards zero while M_z relaxes according to Eq. (2.11).

Resonance phenomena and relaxation effects are described by the Bloch equations

$$\frac{dM_z}{dt} = \frac{M_0 - M_z}{T_1} + \gamma(\mathbf{M} \times \mathbf{H})_z, \tag{2.13}$$

$$\frac{dM_x}{dt} = \gamma(\mathbf{M} \times \mathbf{H})_x - \frac{M_x}{T_2}, \tag{2.14}$$

$$\frac{dM_y}{dt} = \gamma(\mathbf{M} \times \mathbf{H})_y - \frac{M_y}{T_2}. \tag{2.15}$$

In the above equations the resonance excitation in the form of a torque caused by $\mathbf{H}$ has been taken into account. The equations express the fact that in thermal equilibrium under a static field the magnetization wishes to be parallel to H, that is, M_x and M_y have a tendency to vanish. With low non-saturating values of H_{rf} in a coordinate frame rotating at a frequency ω_{rf} and having H_{rf} along the x-axis we get [28]

$$\frac{dM_z}{dt} = -\gamma M_y H_{\mathrm{rf}} + \frac{M_0 - M_z}{T_1}, \tag{2.16}$$

$$\frac{dM_x}{dt} = \gamma M_y \left(H + \frac{\omega}{\gamma} \right) - \frac{M_x}{T_2}, \tag{2.17}$$

$$\frac{dM_y}{dt} = \gamma \left(M_z H_{\mathrm{rf}} - M_x \left(H + \frac{\omega}{\gamma} \right) \right) - \frac{M_t}{T_2}. \tag{2.18}$$

2.2.3 Brief overview of hardware needed for NMR measurements

The NMR magnet is a most important part of the NMR spectrometer. Typically it is an electromagnet made of superconducting wire by winding it in the form of a solenoid. Such NMR magnets produce H fields ranging up to 20 T at maximum, if needed. The magnet must be immersed in liquid helium ($T = 4.2$ K) or cooled by some other methods to achieve temperatures below the superconducting transition

temperature of the wire. To achieve homogeneity and stability of H over space and time, shim coils and field locks can be used, respectively [29].

Inside the NMR magnet, the NMR sample is surrounded by the RF and detection coils which are needed for excitation and signal detection. RF coils can be shaped in many different ways, e.g. as a solenoid coil, saddle coil or wave coil [30]. The excitation coil has to resonate at the NMR frequency, so there must be capacitive elements present in addition to the inductive coil. The resonance frequency of this kind of LC resonator can be calculated, but it must be noticed that the conductivity and the dielectric constant of the sample inside the RF coil also affect it in addition to the values of the coil and the capacitor. In the two-coil configuration the RF and detection coils are in an orthogonal arrangement, to reduce inductive coupling between the coils. In pulsed NMR imaging measurements one coil is sending a pulse into the sample and another is monitoring the voltage induced by the relaxing transverse magnetization after the pulse. It is also possible to have only one coil both generating the oscillating H_{rf} field and measuring the absorbed RF energy. This is often the setup used in cw-NMR measurements although the two-coil arrangement is possible reducing the excitation voltage leaking into the signal amplifier chain. Requirements for the H_{rf} field are the perpendicularity to the H field and the homogeneity over the volume of the sample. Otherwise the amount of magnetization would be different in the different parts of the sample and the measured spectra would deform.

Depending on the required setup, the sample probe can also contain a sample spinner for rotating the sample, temperature controlling circuitry, and gradient coils producing gradients in H.

Our NMR magnet configuration inside the cryostat is presented in Sec. 5.1.1.

2.2.4 Q-factor

Figure 2.2 shows a generalized response curve of a band-pass filter, such as our LC resonator. The filter passes frequencies within a certain range and rejects frequencies outside that range. The bandwidth is defined as the difference between the frequencies at which the energy is half of its peak value, f_l and f_h. In terms of the oscillation amplitude this means that at these frequencies the voltage is

$$V_{\Delta f} = \frac{V_{max}}{\sqrt{2}}. \tag{2.19}$$

The quality factor (Q-factor) of a band-pass filter is defined as the ratio of the resonance frequency to the bandwidth:

$$Q = \frac{f_0}{f_h - f_l} = \frac{f_0}{\Delta f}. \tag{2.20}$$

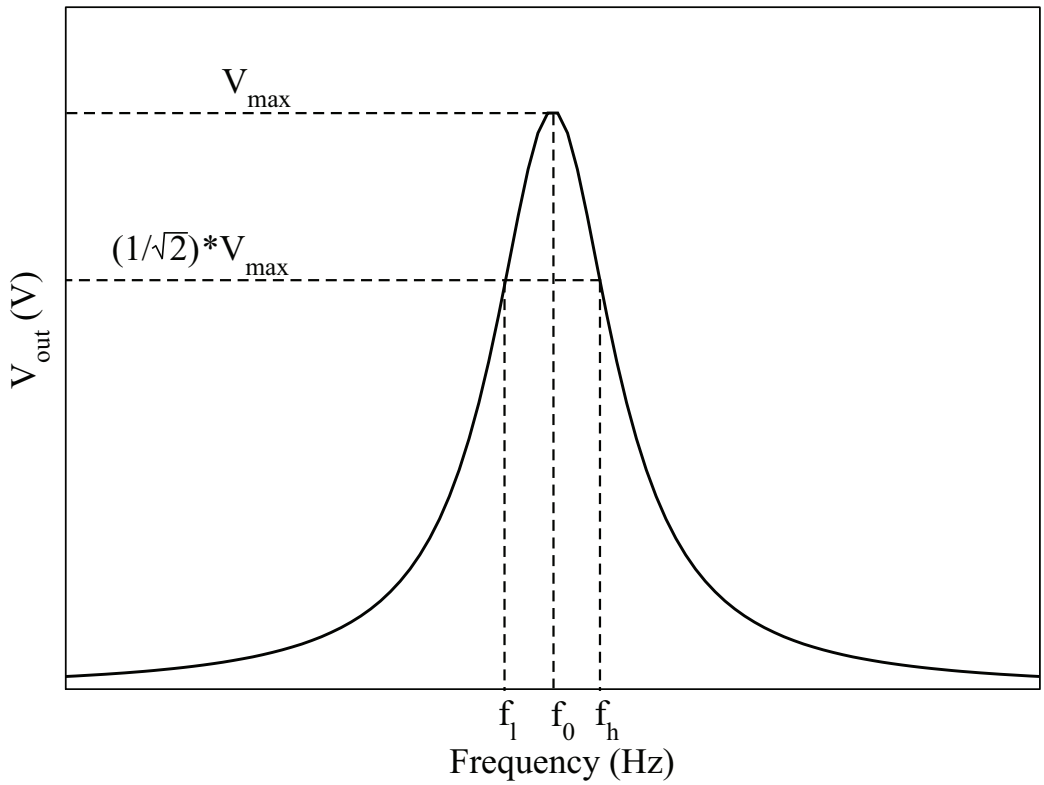

Figure 2.2: *The response curve of a band-pass filter.*

For parallel RLC circuits with discrete components relevant to our setup (R, L and C are all in parallel), the Q-factor can be calculated from the equation

$$Q = R\sqrt{\frac{C}{L}} = 2\pi f_0 CR, \tag{2.21}$$

where R, C, and L are the resistance, capacitance, and inductance of the circuit, respectively.

The resonance frequency f_0 of the parallel RLC circuit can be calculated from

$$f_0 = \frac{1}{2\pi}\sqrt{\frac{1}{LC} + \frac{R_c}{L}}, \tag{2.22}$$

where R_c represents the resistance in series with L, for example the resistance of inductive coil winding constituting L. In many applications R_c is insignificant and can be left out from the equation. For superconducting coils $R_c = 0$.

The Q-factor is an indication of the selectivity of the band-pass filter. The higher the Q-factor, the narrower the bandwidth and the better the selectivity for a given value of f_0. Higher Q-factor resonators also have a higher sensitivity, a

higher resonance amplitude, and a lower rate of energy loss relative to the stored energy of the oscillator. Those are the reasons why we want to find as high a Q-factor as possible for our resonance circuit.

With earlier versions of this setup a Q-factor between $10^4 - 10^5$ was achieved at temperatures below 1 K [10]. The most recent values achieved prior to present updates were less than $2 \cdot 10^4$ at 4.2 K [31]. With a low frequency LC resonator made of discrete components it is possible to achieve even higher Q-factors at cryogenic temperatures, for example 1.8×10^6 [32].

2.2.5 Effect of Q-factor on the output signal

In our cw-NMR measurements, the frequency ω of the RF field is kept constant, while we slowly sweep the strength of the static magnetic field H. In the simplest case we would see the resonance appearing at the Larmor condition (Eq. (2.8)). The complex susceptibility $\chi(\omega)$ of the sample is defined as

$$\chi(\omega) = \chi'(\omega) - i\chi''(\omega), \tag{2.23}$$

where χ' and χ'' are called the dispersion and the absorption susceptibilities, respectively. They are derived from the solutions of the Bloch equations (Eq. (2.13)) [28]

$$\chi'(\omega) = \frac{\chi_0}{2}\gamma H T_2 \frac{(\gamma H - \omega)T_2}{1 + (\omega - \gamma H)^2 T_2^2}, \tag{2.24}$$

$$\chi''(\omega) = \frac{\chi_0}{2}\gamma H T_2 \frac{1}{1 + (\omega - \gamma H)^2 T_2^2}, \tag{2.25}$$

where $\chi_0(p,T)$ is the static susceptibility of the sample and T_2 is the time constant of the decay of the transverse magnetization M_{xy}. The complex susceptibility can be used instead of χ_0 in Eq. (2.10) to get a connection between complex magnetization and magnetic field, where also the phase is included besides the magnitude.

The inductance of the LC resonator is not purely the inductance of the RF coil, L_0. The material inside the coil affects the inductance according to the equation

$$L = L_0(1 + \eta_F \chi), \tag{2.26}$$

where η_F is the filling factor of the setup geometry determining the coupling between the pick-up coil and the sample. There is some voltage u_0 across the resonance circuit when there is no material inside it ($\chi_0 = 0$). When we add the sample inside the RF coil, the voltage u across the resonator is defined as

$$\frac{u - u_0}{u_0} = \frac{-iQ\eta_F\chi}{1 + iQ\eta_F\chi}. \tag{2.27}$$

Assuming that $|Q\eta_F\chi| \ll 1$ applies [4], we see that the detected u is proportional to $Q\eta_F\chi$. Thus the LC circuit with a high Q-factor amplifies the magnitude of the measured signal and the sensitivity of NMR measurements.

At the resonance frequency $\omega = \omega_L = \gamma H$ the dispersion vanishes, $\chi' = 0$, and the absorption is $\chi'' = \frac{\chi_0}{2}\gamma H T_2$. It follows that

$$\frac{u - u_0}{u_0} \approx -Q\eta_F \frac{\chi_0}{2}\gamma H T_2. \tag{2.28}$$

Taking into account that for ^{3}He we have $\gamma = -203.8 \cdot 10^6 \frac{\text{rad}}{\text{sT}}$ and $\chi_0 > 0$, we see that the higher the Q-factor and the filling factor are, the higher is the measured voltage across the resonator at resonance in our measurements.

2.3 NMR in ^{3}He

2.3.1 Theoretical background and textures

In the normal state cw-NMR measurements, resonance absorption occurs at the Larmor frequency (Eq. (2.8)) and no other peaks or anomalies are present (See Fig. 2.3).

The theoretical basis for understanding the NMR line shape in the superfluid phases of ^{3}He is determined by Leggett's equations of motion [33]:

$$\dot{\mathbf{S}} = \gamma \mathbf{S} \times \mathbf{H} + \mathbf{R}_\mathrm{D}, \tag{2.29}$$

$$\dot{\mathbf{d}} = \mathbf{d} \times \gamma (H - \frac{\gamma}{\chi_0}\mathbf{S}) \tag{2.30}$$

where $\mathbf{S}$ is the total spin vector and $\mathbf{d}$ is the order-parameter vector. $\mathbf{R}_\mathrm{D}$ is the dipole torque acting on $\mathbf{S}$ and originating from the spin-orbit interaction [24]. The Leggett equations above together with the expression for $\mathbf{R}_\mathrm{D}$ are enough to describe the spin dynamics of superfluid ^{3}He. The first equation describes the precession of the spin vector and the second of the order-parameter vector.

Magnetic fields, the walls of the container, and externally applied flow all are examples of external perturbations. In the situations where these external perturbations are weak compared to the BCS pairing interaction, the hydrostatic theory can be used to determine the equilibrium properties of superfluid ^{3}He. When several perturbations compete with each other, the formation of a nonuniform distribution of the order parameter is possible. The different distributions are called textures. Since $\mathbf{R}_\mathrm{D}$ and the dynamics of the spin depend on the order parameter, NMR can be used to probe these textures.

In this work we focus only on ^{3}He-B, in which the spatial variations of the rotation matrix $R(\hat{\mathbf{n}}, \theta)$ determine the textures of the order parameter (Eq. 2.1).

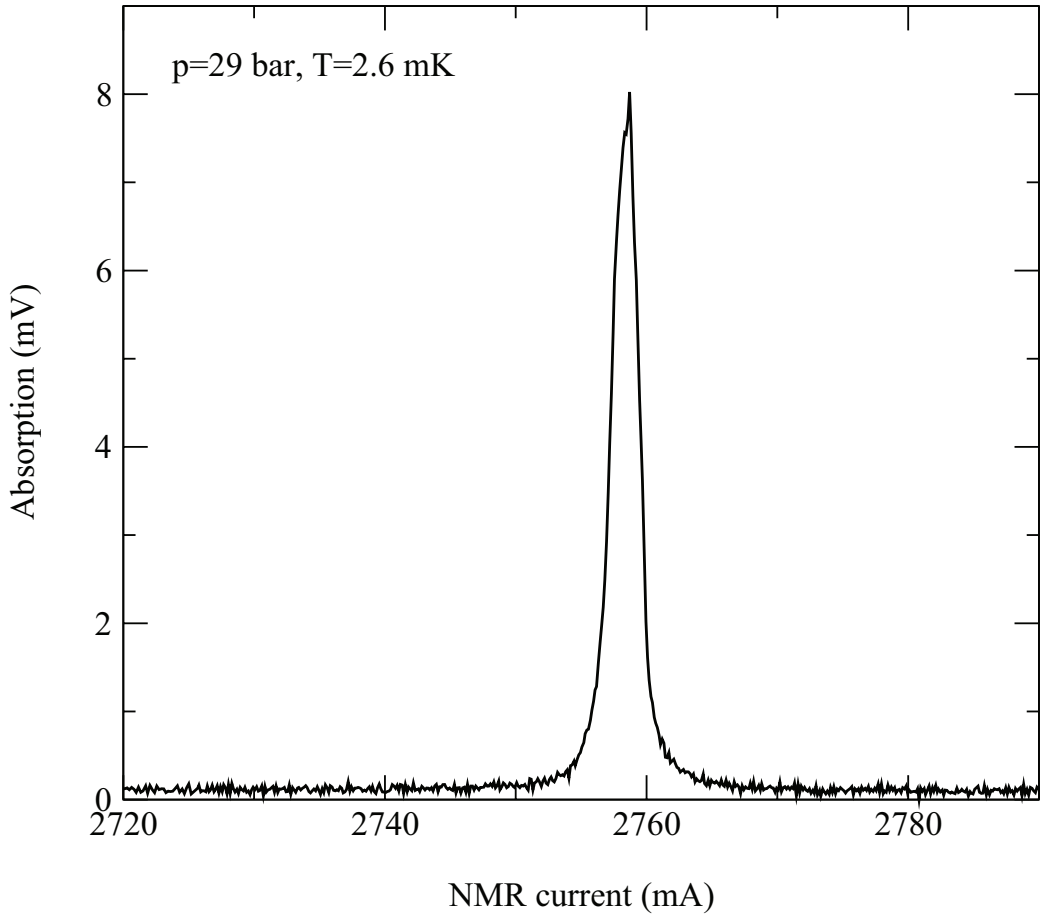

Figure 2.3: *Example of an absorption signal at Larmor frequency measured in the normal phase of liquid ^{3}He at the temperature 2.6 mK.*

The unit vector $\hat{\mathbf{n}}$ points in the direction of the axis around which the spin and orbital coordinate axes have been rotated with respect to each other by the angle θ. The minimization of the dipole interaction requires that the rotation angle (the Leggett angle) $\theta \approx 104^\circ$ [24]. Thus the texture problem is reduced to finding the distribution $\hat{\mathbf{n}}(\mathbf{r})$. The most relevant orientational effects with their respective free-energy contributions affecting the $\hat{\mathbf{n}}$-distribution are presented below. The equilibrium order-parameter texture in ^{3}He-B is determined by minimizing the sum of the individual free-energy contributions. In the B phase the orientational energies are smaller than the dipolar energy and the Leggett angle stays fixed at $\theta \approx 104^\circ$ for cases considered in this work.

An external magnetic field $\mathbf{H}$ induces a small orientational effect on $\hat{\mathbf{n}}$ with a

free energy [34]

$$F_{\rm DH} = -a \int d^3\mathbf{r} (\hat{\mathbf{n}} \cdot \mathbf{H})^2, \tag{2.31}$$

where a is the coupling coefficient and the integration is performed over the volume of the sample. This tends to align $\hat{\mathbf{n}}$ along $\mathbf{H}$. The orienting energy in the presence of counterflow, where the difference $\mathbf{v}_n - \mathbf{v}_s$ between the velocities of the normal and superfluid components is finite on large length scales, has the form [35]

$$F_{\rm HV} = -\lambda_{\rm HV} \int d^3\mathbf{r} (\mathbf{H} \cdot R \cdot (\mathbf{v}_n - \mathbf{v}_s))^2. \tag{2.32}$$

From the equation above, it is conventional to define the dipole velocity $v_{\rm D} = \sqrt{2a/(5\lambda_{\rm HV})} \sim 1$ mm/s. The rigidity of the order parameter texture is described by the gradient energy [34, 36]

$$F_{\rm G} = \int d^3\mathbf{r} \left[\lambda_{\rm G1} \frac{\partial R_{\alpha i}}{\partial r_i} \frac{\partial R_{\alpha j}}{\partial r_j} + \lambda_{\rm G2} \frac{\partial R_{\alpha j}}{\partial r_i} \frac{\partial R_{\alpha j}}{\partial r_i} \right]. \tag{2.33}$$

$F_{\rm DH}$ and $F_{\rm G}$ together determine the length scale of the spatial variations, the magnetic healing length

$$\xi_{\rm H} = \sqrt{65\lambda_{\rm G2}/(8aH^2)}. \tag{2.34}$$

It specifies the rate at which the orientation of $\hat{\mathbf{n}}$ may change in the texture and depends both on the temperature and on the field H. With large values of $\xi_{\rm H}$, compared to the sample size, the orientation of $\hat{\mathbf{n}}$ can change only slowly making the texture look different than with small values of $\xi_{\rm H}$.

Equations (2.31)-(2.33) describe the bulk energies. In addition to these, the walls of the container induce a boundary interaction [34]

$$F_{\rm SH} = -d \int d^2\mathbf{r} (\mathbf{H} \cdot R \cdot \hat{\mathbf{s}})^2, \tag{2.35}$$

where the integration is over the surface of the wall and $\hat{\mathbf{s}}$ is the unit vector normal to the wall pointing towards the superfluid. Another boundary energy arises from the equilibrium spin currents at the surface [37]

$$F_{\rm SG} = \lambda_{\rm SG} \int d^2{\rm r} \hat{s}_j R_{\alpha j} \frac{\partial R_{\alpha i}}{\partial r_i}. \tag{2.36}$$

Finally, we list the orienting interaction arising from the distortion of the bulk state by the vortices [38]

$$F_{\rm LH} = \lambda_{\rm LH} \int_{\rm L} d^3\mathbf{r} (\mathbf{H} \cdot R \cdot \hat{\mathbf{l}}_{\rm V})^2, \tag{2.37}$$

where the integral is to be calculated over the region occupied by the vortices, and $\hat{\mathbf{l}}_V$ is the unit vector of the orientation of the vortex line.

The equilibrium order-parameter texture in ^{3}He-B is determined by minimizing the sum of the individual free-energy contributions in Eqs. (2.31)-(2.37). The different orienting effects described by these textural free-energies are conflicting with each other resulting in an inhomogeneous order-parameter texture ($\hat{\mathbf{n}}$-texture). The coefficients appearing in the free-energy equations can be obtained using the quasiclassical theory of ^{3}He [36, 39].

2.3.2 NMR in non-rotating ^{3}He-B

In the high field limit ($\omega_L \gg \Omega_B$), the transverse resonance frequency in ^{3}He-B is approximately determined by:

$$\omega \approx \omega_L + \frac{\Omega_B^2}{2\omega_L} \sin^2 \beta, \tag{2.38}$$

where $\Omega_B(p,T)$ is the longitudinal resonance frequency in ^{3}He-B (the Leggett frequency), and $\beta(\mathbf{r})$ is the angle between $\mathbf{H}$ and vector $\hat{\mathbf{n}}$. The cw-NMR spectrum is thus formed through the influence of the $\hat{\mathbf{n}}$-texture on the resonance frequency. If $\hat{\mathbf{n}}$ is not parallel to $\mathbf{H}$, the resonance frequency is shifted above the Larmor value. In a non-rotating cylinder (as our sample cell) at our experimental conditions, $\hat{\mathbf{n}}$ forms a continuous axisymmetric distribution over the entire sample known as the simple flare-out texture [34]. At the cylinder axis the magnetic field $\mathbf{H} \parallel \hat{\mathbf{z}}$ orients $\hat{\mathbf{n}}$ parallel to $\hat{\mathbf{z}}$, i.e., $\beta = 0$ and there is no frequency shift meaning that the absorption is at the Larmor frequency. When moving away from the axis, β slowly tends towards the wall- and the flow-dominated value $\beta = \arcsin(\sqrt{4/5}) \approx 63.4°$, which is the maximum value of β occurring in the non-rotating sample. Thus, close to the walls $\sin^2\beta = 0.8$ and the absorption happens at a shifted frequency according to Eq. (2.38). The different values of β are a result of the minimization of the orienting free-energy contributions presented in the previous section (e.g. F_{DH} favors $\hat{\mathbf{n}} \parallel \mathbf{H}$, i.e., $\beta = 0$, whereas F_{HV} and F_{SH} favor an orientation $\beta = 63.4°$).

The overall cw-NMR spectrum of the sample is obtained using the local oscillator model, by considering the fluid as an assembly of uncoupled oscillators with frequencies determined by the local value of axisymmetric $\beta(\mathbf{r})$. The whole NMR line shape is then a distribution of the individual contributions, i.e.,

$$f(\omega) = \frac{1}{V} \int d^3\mathbf{r}\delta[\omega - \omega(\mathbf{r})], \tag{2.39}$$

where V is the volume of the sample [40]. From this it follows that whenever $\beta(\mathbf{r})$ and thus $\omega(\mathbf{r})$ has a constant value over a larger region, the absorption spectrum

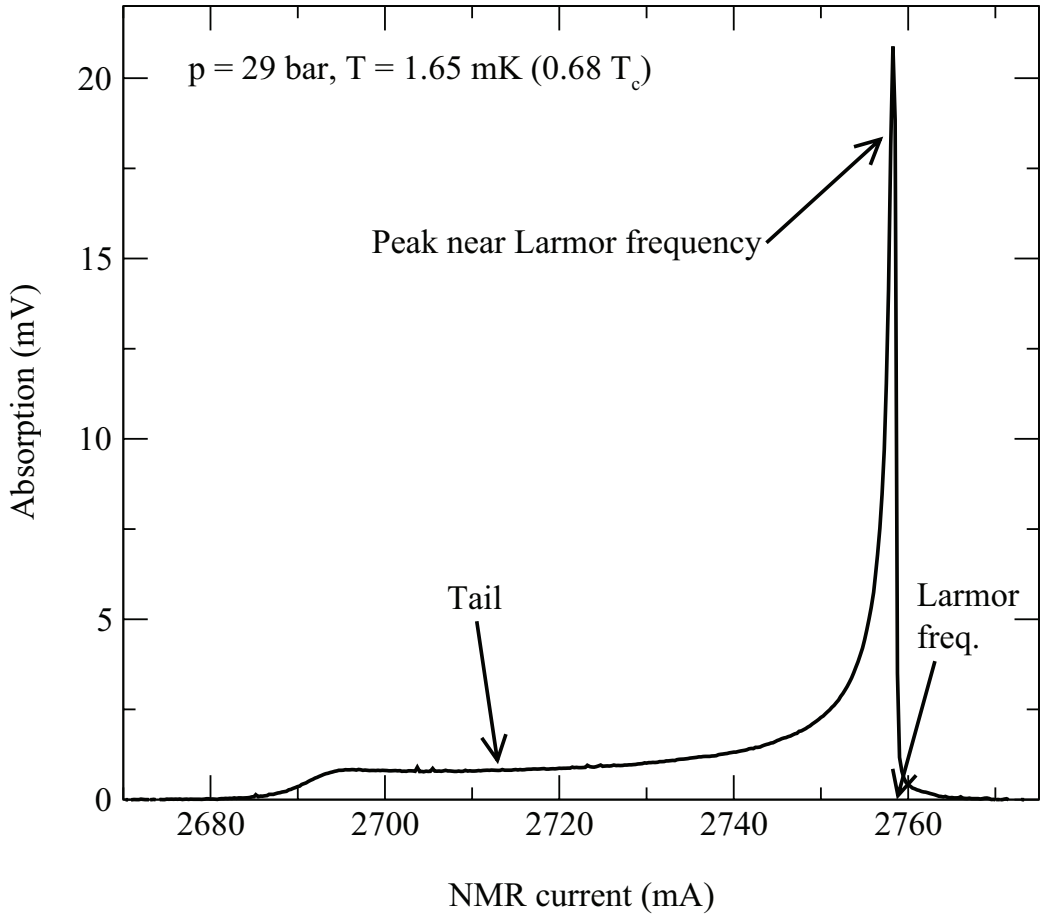

Figure 2.4: *Line shape of the NMR absorption curve measured in superfluid ^{3}He-B when no rotation is applied.*

has a peak at this frequency. When the sample is not rotating (or at low rotation), most of the absorption occurs at frequencies close to the Larmor frequency ω_L ($\beta = 0$). In the case of this simple flare-out texture the spectrum has a peak near the Larmor frequency with a tail caused by the bending of $\hat{\mathbf{n}}$ towards the boundary value $\beta \approx 63.4^\circ$ close to the cylinder wall. An example of this kind of spectrum is seen in Fig. 2.4. This measurement, like all our measurements, is performed by sweeping the NMR field instead of the RF frequency. The magnetic field strength H is directly proportional to the current through the magnet, and so in many cases (like in our figures and calculations) it is just convenient to use directly the measured current instead of the actual field parameters (or to present the results in the frequency scale as described in Sec. 2.3.4). The Larmor frequency f_L marked in the figure is determined from the normal liquid measurements (Sec. 7.1).

In addition to the textural effects, also the inhomogeneity of the external mag-

netic field H causes significant line broadening to the NMR spectra. The Larmor frequency ω_L is spread due to spatial variations in H, and so the transverse resonance frequencies spread according to Eq. (2.38). The average magnetic-field inhomogeneity $\frac{\Delta H}{H}$ can be determined from the NMR signal of the normal liquid (Sec. 7.1). Another source of line broadening is the intrinsic Leggett-Takagi relaxation, arising from the nonequilibrium between the normal and superfluid contributions to the total magnetization [41], and spin diffusion (the movement of atoms to locations with different resonance frequencies).

2.3.3 NMR in rotation

On increasing the angular velocity of rotation in the vortex-free state, a succession of transitions between the different types of textures occurs [42]. With increasing Ω also the counterflow velocity increases since $v_n = \Omega r$ and $v_s = 0$ in the vortex-free state and the absorption begins to accumulate towards the wall- and flow-dominated value $\beta \approx 63.4^\circ$ giving rise to a new peak in the absorption spectrum called the counterflow peak. This texture with the counterflow peak and the peak in the Larmor region is known as the parted flare-out texture and it is separated from the simple flare-out texture by a second order textural phase transition. In Fig. 2.5 two vortex-free spectra at different rotation velocities are seen. We clearly see the difference between the textures as Ω changes. Comparison of these two spectra to the spectrum in Fig. 2.4 is not reasonable because the examples used here are measured with different Larmor frequencies and with different values of excitation voltage. At this point only the general shape of the absorption curves is of interest.

Vortex lines in the B phase can be seen in the NMR signal because of their effect on the global counterflow velocity. They reduce the flow (inside the vortex bundle the average counterflow velocity is zero) and shift the absorption from the counterflow peak at $\sin^2\beta \approx 0.8$ closer to the Larmor frequency at $\beta = 0$ [40]. In the NMR line shape this is seen as an increase in the Larmor region peak height and as a decrease in the counterflow peak height. It is even possible to resolve the effect of a single vortex line on the spectrum [12].

More NMR spectra with different rotation velocities and textures are presented in Sec. 7.3.

2.3.4 Relation between field and frequency in NMR of ^{3}He-B

The cw-NMR measurements can be done either by changing the RF frequency or the magnetic field H. In this section we present the way to convert the results achieved in one scale to the another scale. The exact equation for the transverse

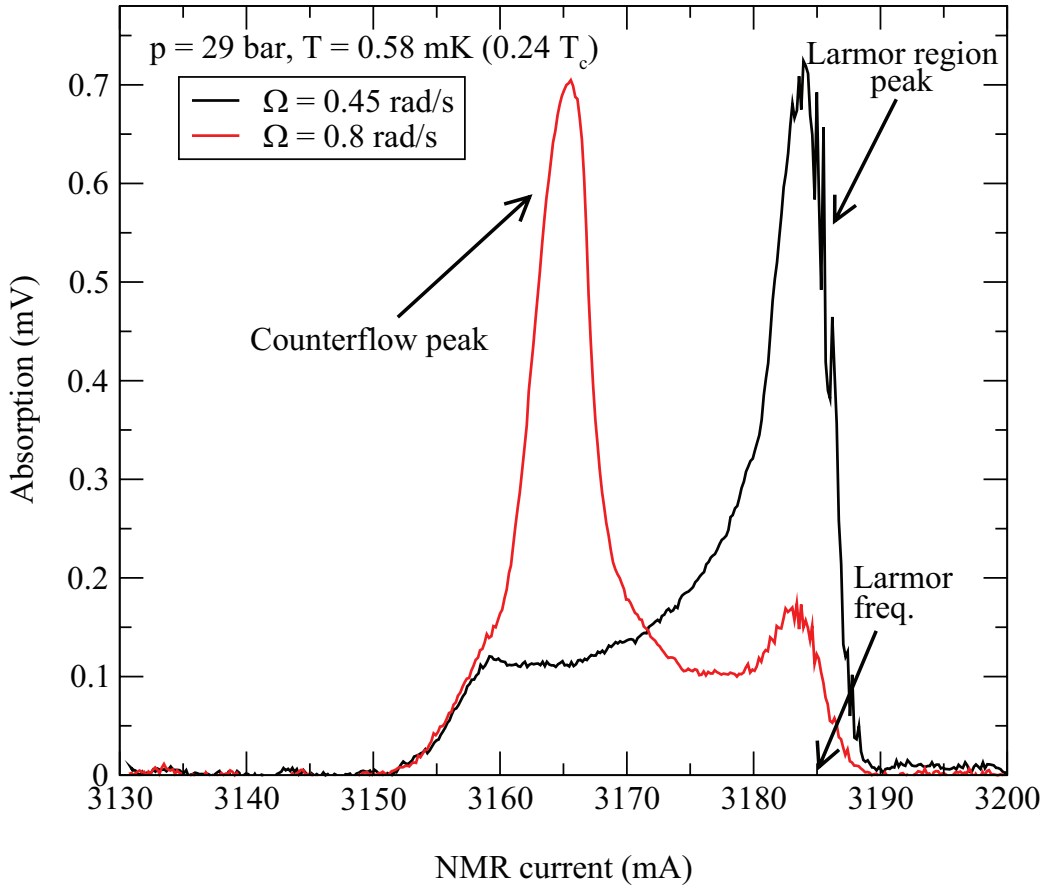

Figure 2.5: *Two example spectra at different rotation velocities showing the line shapes of the simple and the parted flare-out texture.*

resonance frequency f_β as a function of the longitudinal resonance frequency $f_B(p,T)$ is [24]

$$f_\beta^2 = \frac{f_L^2 + f_B^2}{2} + \sqrt{\left(\frac{f_L^2 + f_B^2}{2}\right)^2 - f_L^2 f_B^2 \cos^2\beta}. \tag{2.40}$$

With variable exchanges $f_L \to f_\beta\sqrt{x}$ and $f_B \to f_\beta\sqrt{y}$ we get

$$x + y + \sqrt{x^2 + y^2 - 2xy\cos(2\beta)} = 2. \tag{2.41}$$

From this we can solve x:

$$x = \frac{y-1}{\cos^2\beta \cdot y - 1}. \tag{2.42}$$

If the longitudinal magnetic field H is swept (marked as H_β) in the cw-NMR measurements while the transverse RF field has a constant value f_{rf}, we have

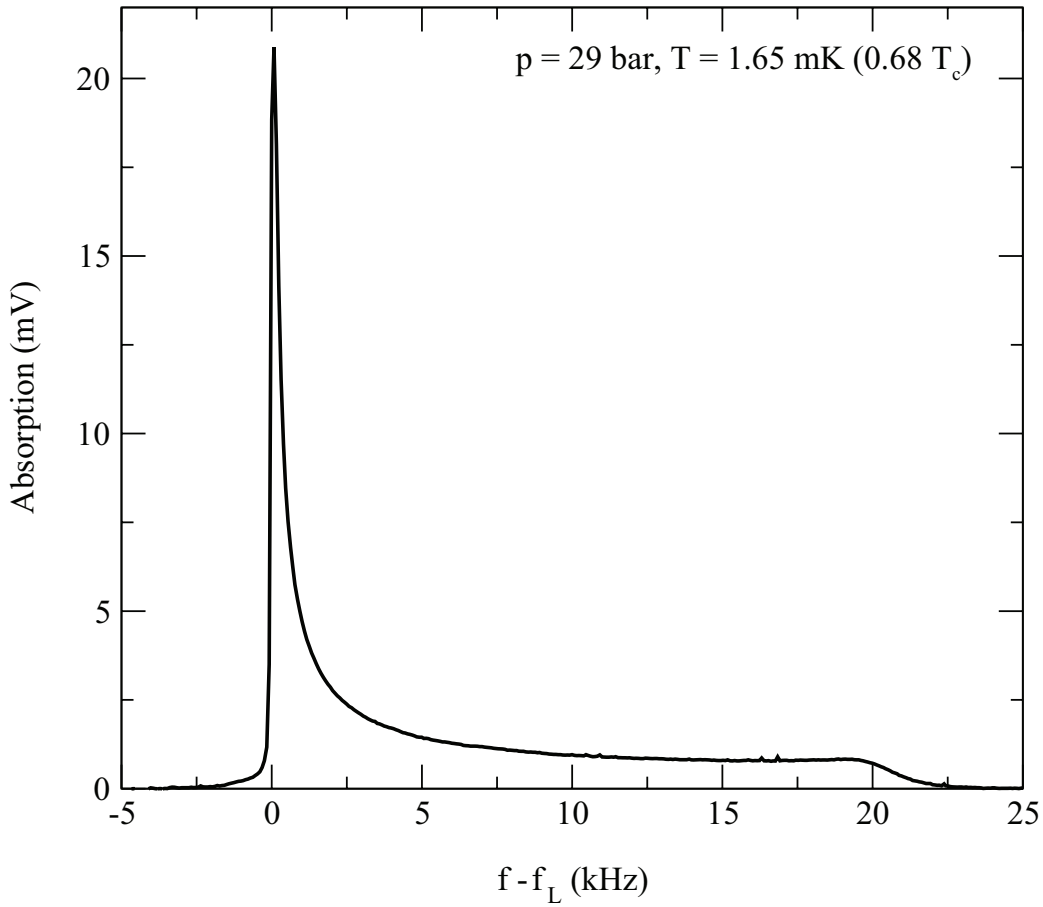

Figure 2.6: *The NMR absorption curve from Fig. 2.4 converted to frequency scale.*

$f_\beta = f_{\rm rf}$ and $f_L = \gamma H_\beta$. Taking this into account we get $\sqrt{x} = \frac{f_L}{f_\beta} = \frac{\gamma H_\beta}{f_{\rm rf}} = \frac{H_\beta}{H_L}$, where H_L is the field satisfying the Larmor condition (here $f_{\rm rf} = \gamma H_L$). This results in

$$H_\beta = \sqrt{\frac{f_{\rm B}^2 - f_{\rm rf}^2}{\cos^2\beta \cdot f_{\rm B}^2 - f_{\rm rf}^2}} H_L. \tag{2.43}$$

After this we get the correspondence between $f_{\rm rf}$ and H_β by substituting the H-sweeping conditions to Eq. (2.40):

$$f_{\rm rf}^2 = \frac{f_{\rm B}^2 + \gamma^2 H_\beta^2}{2} + \sqrt{\left(\frac{f_{\rm B}^2 + \gamma^2 H_\beta^2}{2}\right)^2 - \gamma^2 f_{\rm B}^2 H_\beta^2 \cos^2\beta}. \tag{2.44}$$

An exactly equal situation is the one where the transverse frequency f_β is swept while the field H has a constant value H_L. Then we have $f_L = \gamma H_L$ and

$$f_\beta^2 = \frac{f_B^2 + \gamma^2 H_L^2}{2} + \sqrt{\left(\frac{f_B^2 + \gamma^2 H_L^2}{2}\right)^2 - \gamma^2 f_B^2 H_L^2 \cos^2\beta}. \tag{2.45}$$

Finally, we want to express f_β via H_β from the equations above assuming that $\cos\beta$ is the same. The resulting equation is

$$f_\beta^2 = \frac{1}{2}\left(f_B^2 + f_{rf}^2 + \sqrt{\frac{(f_B^2 - f_{rf}^2)((f_B^2 + 3f_{rf}^2)H_\beta^2 - 4f_{rf}^2 H_L^2)}{H_\beta^2}}\right). \tag{2.46}$$

Let us mark the field corresponding to $\cos^2 = \frac{1}{5}$ (which corresponds to $\beta \approx 63.4°$) as H_e and Eq. (2.43) transforms to

$$f_B^2 = \frac{5\left(f_{rf}^2 H_e^2 - f_{rf}^2 H_L^2\right)}{H_e^2 - 5H_L^2}. \tag{2.47}$$

Combining the two above equations we get

$$f_\beta^2 = \frac{f_{rf}^2\left(3H_e^2 - 5H_L^2 - 2H_e\sqrt{\frac{5H_L^4}{H_\beta^2} + H_e^2\left(2 - \frac{H_L^2}{H_\beta^2}\right) - 5H_L^2}\right)}{H_e^2 - 5H_L^2}. \tag{2.48}$$

Simplifying this we get the approximate expression (omitting all 3rd order terms and higher) between the frequency and field scales:

$$\frac{f_\beta - f_{rf}}{f_{rf}} = \frac{\delta f}{f_{rf}} = \frac{\left(H_L - H_\beta\right)H_\beta}{H_L^2}. \tag{2.49}$$

The difference between the exact transformation (Eq. (2.48)) and the approximate expression (Eq. (2.49)) is at maximum less than 1‰. Figure 2.6 shows the same data as Fig. 2.4 as a function of the frequency difference δf from the Larmor frequency instead of the current used to create field H.

2.3.5 Temperature measurement from the NMR spectrum

The longitudinal resonance frequency of ^{3}He-B, $f_B(p,T)$, depends on pressure and temperature. We can write Eq. (2.42) in the form

$$x = \frac{(\frac{f_B}{f_L})^2 - 1}{\cos^2\beta \cdot (\frac{f_B}{f_L})^2 x - 1}, \tag{2.50}$$

where we have taken into account that $y = (\frac{f_B}{f_\beta})^2 = (\frac{f_B}{f_L})^2 x$. As a result we get for f_B

$$f_B^2 = \frac{f_L^2(1-x)}{x(1-x\cos^2\beta)}. \tag{2.51}$$

Using the above equation we can solve f_B which corresponds to a certain transverse resonance frequency f_β or a field H_β. Remember that $x = (\frac{f_L}{f_\beta})^2 = (\frac{H_\beta}{H_L})^2$, when sweeping H.

In Fig. 2.4 we see the NMR absorption spectrum when no rotation is applied. There are two distinguishable parts in the spectrum: the peak near the Larmor edge and the end of the long tail. They correspond to situations $\sin^2\beta \gtrsim 0$ and $\sin^2\beta = 0.8$, respectively (See Eq. (2.38)). Thus the end of the tail is in a precisely determined place which gives us the possibility to determine f_B and the corresponding temperature. By fitting a straight line to the end slope of the tail and determining the point where the line crosses the baseline we get the frequency f_β (or current H_β) corresponding to the surface value $\sin^2\beta = 0.8$. Substituting this value to Eq. (2.51) we get $f_B(p,T)$ which we can convert to temperature using the experimental data gathered e.g. in Ref. [43] which gives values down to $0.3\,T_c$ at various pressures. Below that f_B saturates and loses its sensitivity as a suitable tool for temperature measurements. In the example figure the temperature determined in this way from the spectrum is $0.68\,T_c$ which agrees with the measured value from the ^{3}He melting curve thermometer (MCT) [4, 44]. It is convenient to calculate the temperature from the non-rotating spectrum because rotation modifies the texture. However, at high enough rotation velocities the counterflow peak is at $\sin^2\beta = 0.8$ which gives the possibility to do precise temperature measurements again from the NMR spectrum.

Chapter 3

Cryogenic GaAs MESFET preamplifier

3.1 The basis of preamplifier design

We want to use a cryogenic preamplifier close to the signal source because this way we can effectively isolate the sensitive experiment at low temperatures from capacitive, resistive, and mechanical interference in the output line to room temperature. The preamplifier should also be connected directly to the superconducting high-Q LC resonator with superconducting wires to minimize resistive losses. It is also crucial to have a preamplifier with high input impedance not to load the high-Q tank circuit and to make use of the signal amplification with the high Q resonator. With this kind of setup high amplitude sensitivity should be possible to achieve.

For amplifiers at LHe-temperatures and below, the GaAs MESFETs are the suitable solution. They can be operated from room temperature down to LHe temperatures [45, 46]. The problem with alternative Si FETs is that they suffer from charge carrier freeze-out below 50 K.

3.2 Preamplifier circuit properties

3.2.1 Circuit diagram and components

The circuit diagram of our preamplifier is shown in Fig. 3.1. It is a two-stage amplifier constructed from two FETs. The lower FET (input stage) operates in a common source configuration and drives the upper FET (output stage) which is connected as a common gate. This so called cascode design was chosen to minimize coupling between the amplifier input and output. The cascode arrangement

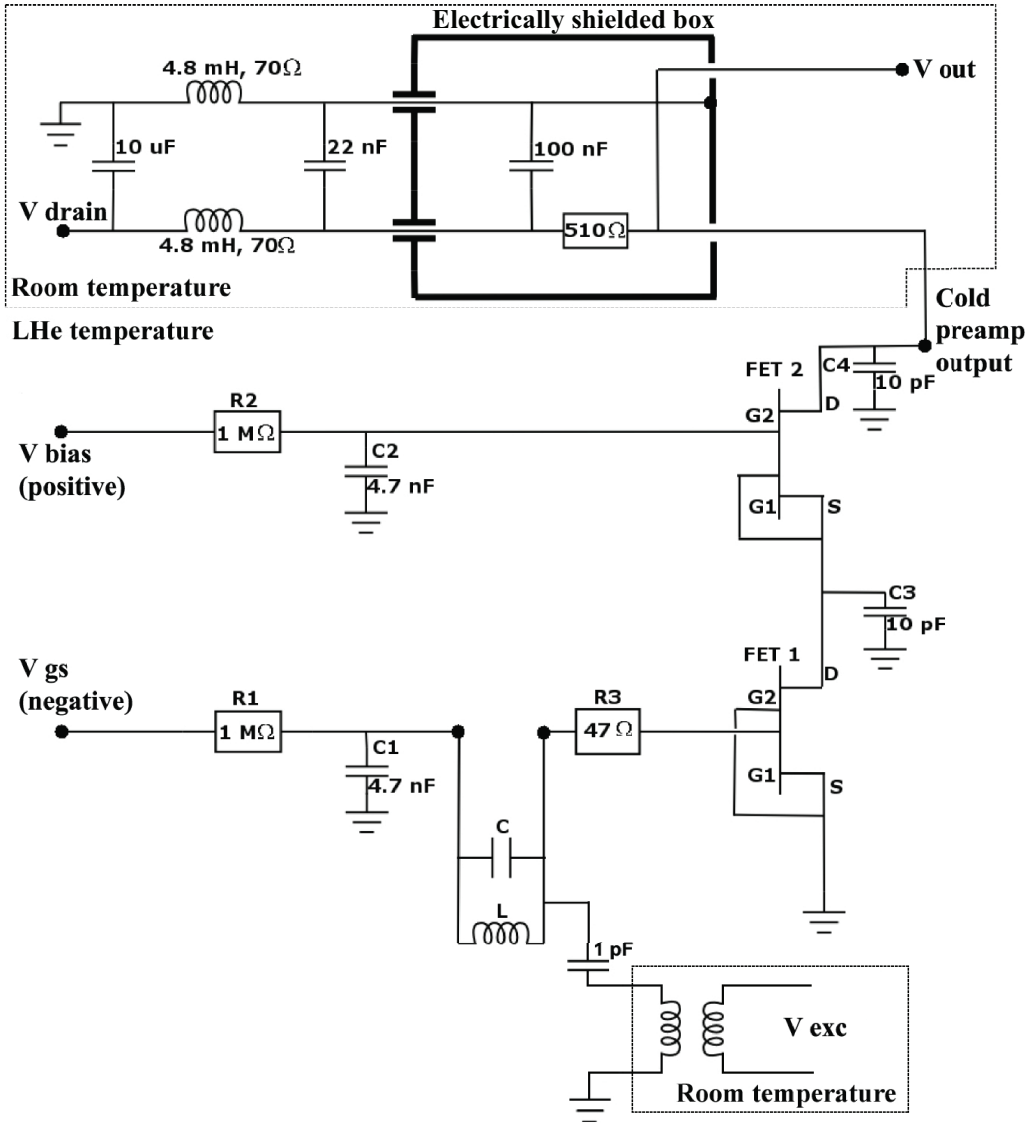

Figure 3.1: *Circuit diagram of the cooled GaAs MESFET preamplifier. Also the room temperature circuitry is shown including the isolation transformer connected to the oscillator supplying the excitation signal.*

is very stable. Ideally the lower FET has unity voltage gain and nearly constant voltage along the source-drain channel. Thus there is essentially nothing to feed back into its gate. The upper FET has nearly constant voltage at its gate and source. The result is that only nodes with significant voltage on them are the input and the output of the cascode state, i.e., the gate of the lower FET and the drain of the upper FET, respectively. Input and output are separated by the central connection of nearly constant voltage between the FETs and by the physical distance of them. This way the additional positive feedback, which might restrict the stability of the amplifier and introduce extra noise, is reduced.

We use two dual-gate Sony 3SK166 n-channel GaAs MESFETs in our preamplifier. They are designed for UHF band low-noise amplification and thus have small feedback gate-drain capacitance C_{gd}, typically only 25 fF. Their miniature surface mount package provides good thermal anchoring and control of stray capacitances. The feedback of the cascode stage is not completely eliminated if the two FETs do not have exactly the same forward transfer admittance g_m. Because in practice the FETs are not identical, the gate bias voltage of the upper FET should be used to set the voltage gain of the lower FET to the desired level of 1 to minimize feedback. These FETs have two gates, but the second gate is unnecessary and is connected directly to the source.

In the cascode design also the input capacitance due to the Miller effect is minimized (Section 3.2.2). It also offers high input impedance and so allows us to connect the preamplifier directly to the high impedance LC resonance circuit (Section 3.2.4).

Capacitors C1 and C2 are surface mount type 4.7 nF American Technical Ceramics (ATC) 700B series NP0 ceramic multilayer capacitors. They are low noise temperature-independent capacitors used to filter the AC-noise from the DC bias voltages. C3 and C4 are surface mount type 10 pF ATC 100B series ultra stable high-Q porcelain multilayer capacitors. They limit the bandwidth by providing a low impedance ground for high frequency signals and ensure the stability of the circuit at high frequencies.

For filtering resistors R1, R2 and R3 the absolute value of resistance is not very important. R1 and R2 protect the FET gates. R3 together with the FET1 input capacitance C_{gd} works as a low pass filter eliminating the high frequency parasitic oscillation (Section 3.2.3). They all are surface mount type, size 0805. The 1 MΩ resistors R1 and R2 have been manufactured by Phycomp (Yageo) and the 47 Ω R3 has been manufactured by Panasonic.

The upper FET drives the 510 Ω load resistor, across which the final output signal is measured. The room temperature part of the circuit is included in the voltage source designed by Roch Schanen [47]. The bias voltages V_{gs} and V_{bias} and the drain voltage V_{drain} are also supplied from this source. Circuit diagrams for these sources are shown in Figs. 3.2, 3.3 and 3.4. To avoid C2 discharging

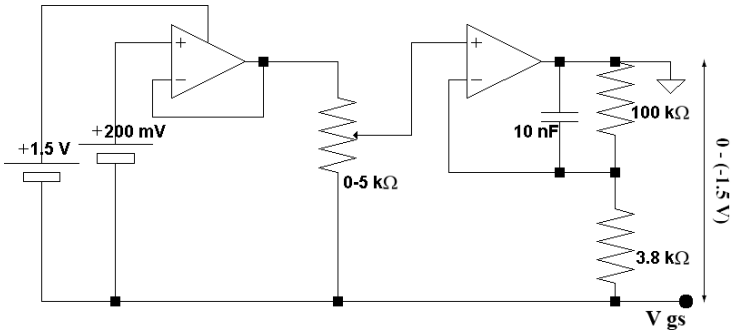

Figure 3.2: *Negative gate voltage source for FET1. The 200 mV reference voltage and the two operating amplifiers are provided by the LM10CN chip.*

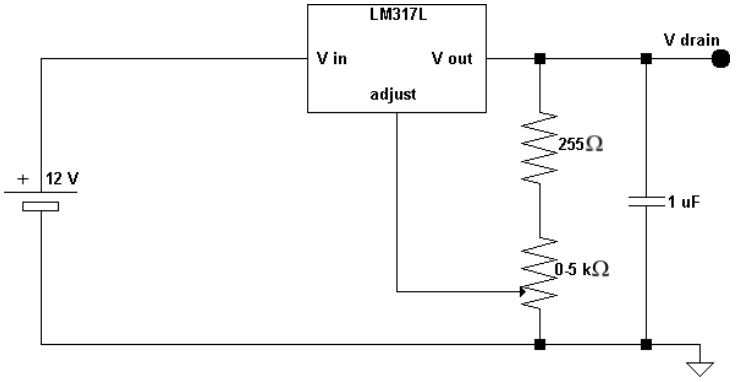

Figure 3.3: *Voltage source for V_{drain}.*

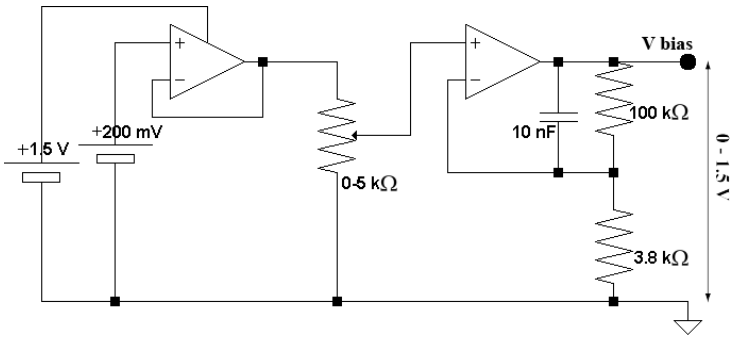

Figure 3.4: *Positive gate voltage source for FET2. The 200 mV reference voltage and the two operating amplifiers are provided by the LM10CN chip.*

through the gate-channel junction of the upper FET and short-circuiting it when the amplifier is switched off, the bias and drain voltages must be switched off in the right order: first switching off V_{bias}, then V_{drain}, and finally V_{gs} [10]. At switch on the order is reversed: V_{gs}, V_{drain}, and V_{bias}.

3.2.2 Miller effect

The Miller theorem suggests that in situations with stray capacitance between the amplifier input and output, this capacitance effectively appears as a capacitance from input to ground and can be expressed as

$$C_{Miller} = C(1 + A_v), \tag{3.1}$$

where C is the physical capacitance between amplifier input and output, and A_v is the absolute voltage gain of the amplifier [48]. In FETs there are internal capacitances, for example between the gate and drain, so the FET operating in a common source configuration is affected by the Miller effect.

In our preamplifier the cascode design is used. The upper FET works as a very low input impedance for the lower FETs output (drain). The upper FET's gate is biased with fixed voltage preventing its source voltage (lower FET's drain voltage) from swinging. This makes the voltage gain of the lower FET very low, so minimizing the Miller capacitance between its gate and drain. The loss of voltage gain is recovered by the upper FET, which has a common gate connection and thus does not suffer from the Miller effect. Eliminating the Miller effect in FETs reduces the attenuation of high frequencies and so contributes to a higher bandwidth [49].

3.2.3 Parasitic oscillations and capacitive coupling

Parasitic oscillation is defined as any unwanted oscillation occurring at a frequency well outside the amplifier's passband. It is normally occurring at higher frequencies and is observed as fuzziness on part of the output waveform, erratic current-source operation, unexplained op-amp offsets, or circuits that behave normally with the oscilloscope probe applied, but go wild when the scope is disconnected. Over-voltage transients, radio frequency noise emission, high switching losses, and even uncontrolled sustained oscillation and destruction of devices because of parasitic oscillation are possible. Parasitic oscillation can be caused for example by unintended Hartley or Colpitts oscillators (Fig. 3.5) which make use of lead inductances and interelectrode capacitances. In case of FETs, parasitic oscillation is most easily detected on the gates but also exists in the drain currents and drain voltages [49, 50]. It can be very intermittent and may occur with the same

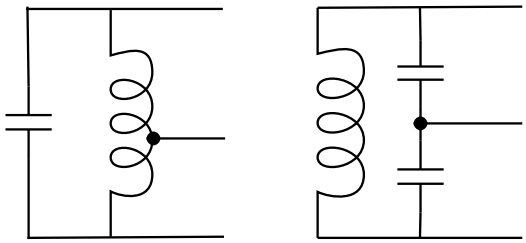

Figure 3.5: *The Hartley oscillator on the left is an LC oscillator that derives its feedback from a tapped coil (or two coils in series) in parallel with a capacitor. The Colpitts oscillator on the right consists of one coil and a capacitive voltage divider.*

components in one circuit but not in another due to differences in circuit layout. High frequency parasitic oscillations degrade the performance at low frequencies, produce extra heat leak to the experiment, and are especially troublesome with active high-frequency GaAs semiconductor components.

In our setup there is the possibility of creating a Colpitts oscillator from the resonator circuit and the internal capacitances of the lower FET. Also the FETs alone create a possible RLC-oscillator involving the capacitances of FET frames, the parasitic inductances of connection leads, and the gate resistances. Increasing the gate resistance damps the oscillation and is often effective in preventing it in the first place. Resistor R3 close to the gate of FET1 serves for that purpose. On top of that, the high-Q low loss capacitor C1, which determines the bandwidth between the FETs, provides a low impedance ground for high frequency signals.

Parasitic capacitive coupling occurs when two signal lines are close to each other and causes what appears to be noise. To reduce coupling, signal-carrying wires or conductors on a circuit board are usually separated as far from each other as possible, or ground lines or ground planes are placed between signals that might affect each other. On our preamplifier circuit board the input and output sides are isolated as far from each other as possible taking the available space into consideration. The back side of the circuit board is copper which is grounded to the preamplifier box to increase the shielding of the signal lines and to reduce the coupling between them. For the same reason all shielding jackets of the signal transfer wires are connected to the same ground potential.

3.2.4 Impedance matching

Impedance matching means adjusting the impedances of the components in the circuit so that they work well together. Setting the input impedance of an electrical load (Z_{load}) exactly to the same value as the output impedance of the signal source

(Z_{source}) maximizes power transfer by minimizing the reflections from the load to the source. In low-frequency or DC systems, or in systems with purely resistive sources and loads, the reactances are negligible or zero. In this case, maximum power transfer occurs when the resistance of the load is equal to the resistance of the source. For reactive components the maximum power transfer is obtained when

$$Z_{load} = Z^*_{source}, \tag{3.2}$$

where * indicates the complex conjugate [51]. For two impedances to be complex conjugates, their resistances must be equal, and their reactances must be equal in magnitude but of opposite sign.

The condition of maximum power transfer does not result in maximum efficiency. Efficiency η is defined as the ratio of power dissipated by the load to power developed by the source, and for resistive elements it can be written as

$$\eta = \frac{R_{load}}{R_{load} + R_{source}}. \tag{3.3}$$

From this we see that, for example, if $R_{load} = R_{source}$, then $\eta = 0.5$. So the efficiency is not maximized simultaneously with the power transfer. The maximum efficiency, $\eta = 1$, is achieved when $R_{load} = \infty$ or $R_{source} = 0$.

If a low impedance source is connected to a high impedance load, the power that can pass through the connection is limited by the higher load impedance. However, the voltage transfer to the load is higher and less prone to distortion and electromagnetic interference than if the impedances were matched. With high enough load impedances almost no power is transferred, and the load device does not appreciably load the source device. In situations where the load impedance is ten times or more than the source impedance, this maximum voltage connection is called impedance bridging. It is used in applications where maximizing the transfer of the voltage (and also the efficiency) is more important than maximizing the power transfer.

The resonator is connected to the cascode stage of the preamplifier. The lower FET in the cascode design has a high input impedance because it is operated in the common source configuration, and also its noise optimum signal source impedance is high (impedance measurements in [10]). This allows the cascode stage to be driven by a high impedance source (like the parallel LC circuit in resonance) with minimum loss in signal quality.

The sine wave excitation is fed to the preamplifier at LHe temperature from a frequency generator through a low-impedance transformer at room temperature. The secondary of the transformer works as a low impedance voltage source, which is connected via a small coupling capacitor $C_{exc} = 1$ pF to the resonance circuit. Together with the high impedance LC resonator the transformer forms an

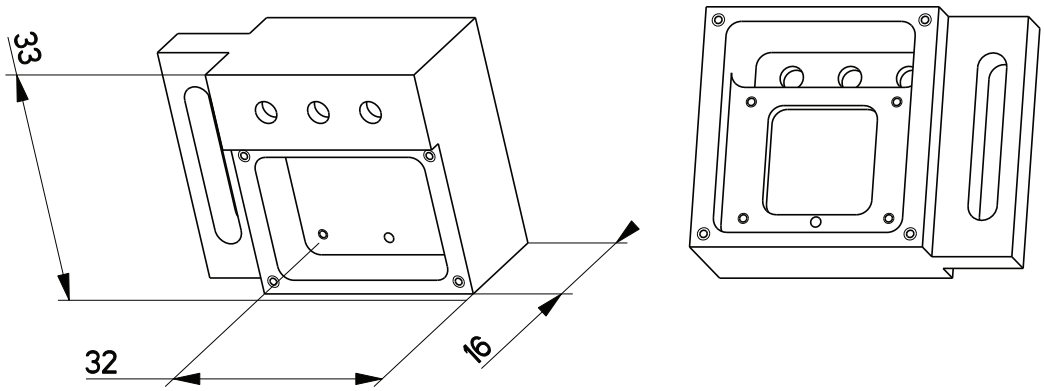

Figure 3.6: *Preamplifier casing seen from both sides without the closing caps. The large holes are for the connectors.*

impedance bridging connection at the resonant frequency maximizing the transfer of voltage from the transformer. The coupling capacitor blocks the DC voltage V_{gs} from passing through the transformer winding to ground. The capacitor also couples the excitation signal and the resonator weakly due to the big impedance difference, which has proven to offer stable operation and not to load the Q-factor.

3.3 Preamplifier casing and connections

The preamplifier and the coupling capacitor are housed inside copper boxes plated with a 5 μm thick gold layer. The boxes are milled on the two sides of a copper slab (Fig. 3.6): the coupling capacitor is on one side and the circuit board containing the actual preamplifier is on the other side of the slab. The component layout on the board is presented in Fig. 3.7. The input and the output are separated as far from each other as possible and the bottom side of the preamplifier board is grounded to the box to reduce the parasitic capacitive coupling (section 3.2.3). The soldering pads are gold plated copper. Compared to the previous design (See [31]) the size of the preamplifier is now bigger for better input-output isolation, to enable the use of more rigid larger size threaded connectors, and for more convenient handling.

The input and output connectors in the preamplifier box (7 connectors in total) are Ultra Miniature (LEPRA/CON) RF Connectors from Tyco Electronics. The advantages of these connectors is their small size and the threaded connection mechanism. Threaded connectors offer better reliability and mechanical stability than the snap-on connectors used before.

Inside the casing all the wires from the connectors to the preamplifier circuit board are superconducting NbTi/Cu-wires with a diameter $\varnothing = 170\,\mu$m. The wires

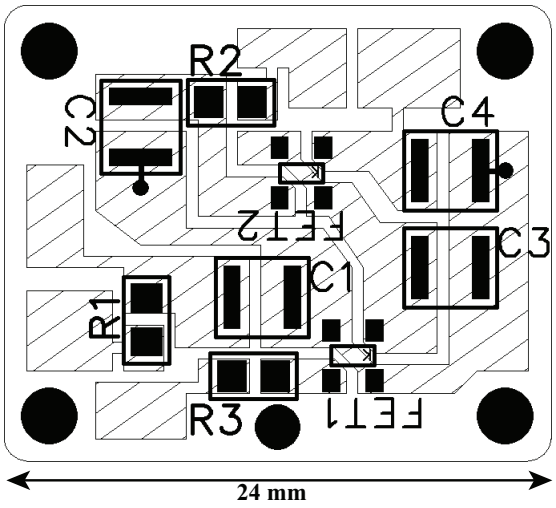

Figure 3.7: *Component layout on the preamplifier circuit board located inside the preamplifier housing box. Striped areas represent the conducting gold plated copper areas. Outlines and connecting pads of parts are marked in black. Big black circles are holes for the fixing screws and for the wire input.*

to the LC-circuit as well as the excitation and the output wires outside the casing are superconducting NbTi/CuNi-wire ($\varnothing = 50\,\mu$m) protected with a grounded metal jacket. Similar superconducting wire as a twisted pair and with a grounded metal jacket protection is used for V_{gs} and V_{bias}.

Chapter 4

High Q LC resonance circuit

Our high-Q resonance circuit consists of one capacitor with capacitance C and one superconducting coil with inductance L connected in parallel. In resonance, the reactances of the coil and the capacitor cancel each other out and the resonator impedance is at maximum. In theory, the impedance would even be infinite if the coil and the capacitor had no losses, but in practice there are always losses, for instance in the form of the series resistance of the coil wire and the parallel resistance of the capacitor insulation. The series resistance of the superconducting coil can be assumed to be close to zero, whereas the parallel resistance of the resonator is increased by the signal source and the preamplifier input. So in resonance, the impedance of the parallel RLC resonator is purely resistive equaling the total parallel resistance R. The existence of the parallel resistance means that the impedance of the circuit, and thus the Q-factor, are finite. For example with the values $Q = 10000$, $C = 1\,\mathrm{nF}$, and $f_0 = 1.0\,\mathrm{MHz}$, we get using equations (2.21) and (2.22) a resistance $R = 1.6\,\mathrm{M\Omega}$.

The resonator is connected to the cascode stage of the preamplifier. Both the resistive part R_{gs} and the reactive part C_{gs} of the input impedance of the MESFET depend on the bias voltage V_{gs}. With our n-channel FETs the more negative the bias voltage is the smaller C_{gs} is and the higher R_{gs} is. The resistive part is parallel to the resonance circuit and loads directly the Q-factor. The optimal situation is to have as high R_{gs} as possible because the higher the parallel resistance in a parallel RLC circuit, the smaller the loading and the higher the Q-factor (Eq. 2.21). Q-factor measurements with different values of V_{gs} can be found in Ref. [10]. It can be seen that with our FETs the Q-factor does not actually rise with a more negative V_{gs} meaning that also some other sources of loss are present.

We are using two independent spectrometers in parallel with different resonance frequencies, and thus different coils and capacitors are used in them. The coils are split solenoid type coils wound from superconducting $50\,\mu$m multifilament NbTi/CuNi Niomax wire. The dimensions and the shape of the coil formers

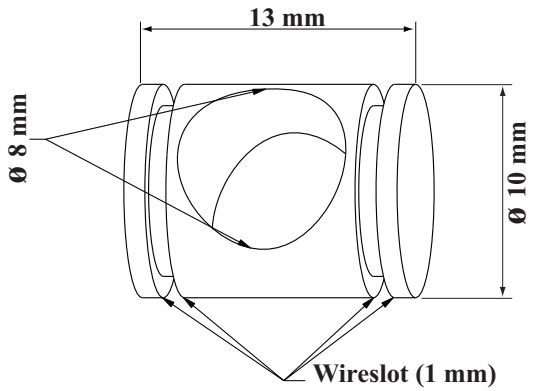

Figure 4.1: *Coil holder and its dimensions.*

Table 4.1: *Specifications of the resonance circuits in spectrometers A and B.*

Spectrometer	coil - layers:turns	$L_{T_{room}}$ (μH)	$R_{T_{room}}$ (Ω)	C (pF)	$f_{L,T_{LHe}}$ (MHz)
A (top)	2:30+30	37.2	462	1000	0.865
B (bottom)	1:15+15	12.7	287	754	1.967

can be seen in Fig. 4.1. These have been machined from fused quartz. Table 4.1 shows the specifications of the coils.

Together with the coils, two different capacitor banks are used to tune the resonance frequencies close to the chosen Larmor frequencies of the A and B spectrometers. The values of these capacitor banks can be seen in Table 4.1. In spectrometer A, one 1000 pF capacitor is in use, and spectrometer B uses three 220 pF capacitors and one 47 nF capacitor in parallel. All the capacitors are surface mount type American Technical Ceramics (ATC) series 100B porcelain high Q multilayer capacitors.

Earlier, coils of different size and different coil-capacitor combinations were tested in my special assignment [31]. Differently shaped coils, namely saddle and wave coils, have been tested by Sakari Arvela in his special assignment report [30].

Chapter 5

Rotating cryostat and measurement setup

5.1 ROTA cryostat

The superfluid ^{3}He measurements are carried out in a rotating nuclear demagnetization cryostat. Low temperatures are achieved using a combination of a dilution refrigerator for precooling and a nuclear adiabatic demagnetization stage. Rotation is needed for creating vortices in the sample. The physics behind the refrigeration and the detailed description of the structure of our cryostat can be found in Refs. [1, 4, 5]. At present, temperatures as low as 500 μK in the sample and rotation speeds of about 3 rad/s are achievable. For the present measurements we changed many of the connectors in the devices and between the coaxial cables to screwed SMA and SMC connectors instead of BNC and snap-on MMCX connectors to reduce the interference caused by the vibrations. For the same reason a substantial part of the room temperature wiring is now provided with semi-rigid coaxial cables (Huber+Suhner EZ_86_TP_M17, $\varnothing$2.2 mm) instead of flexible cables.

We use two spectrometers, A (top) and B (bottom), with different resonance frequencies (See section 4). The NMR pick-up coils are fixed around a quartz cylinder filled with ^{3}He and pressurized up to 29 bar. The geometry is shown in Fig. 5.1. The pick-up coils both create the transverse excitation field $H_{\rm rf}$ and probe the sample (See Sec. 2.2). The ^{3}He cylinder is in thermal contact with the nuclear stage through a sintered copper powder heat exchanger. The coils have a 90° displacement in their orientations (See Fig. 5.1), to reduce mutual interference between them. The NMR magnet system is situated around the sample assembly as described in Sec. 5.1.1. All superfluid measurements discussed in this thesis have been performed in the B phase of ^{3}He. Two quartz tuning forks on the bottom

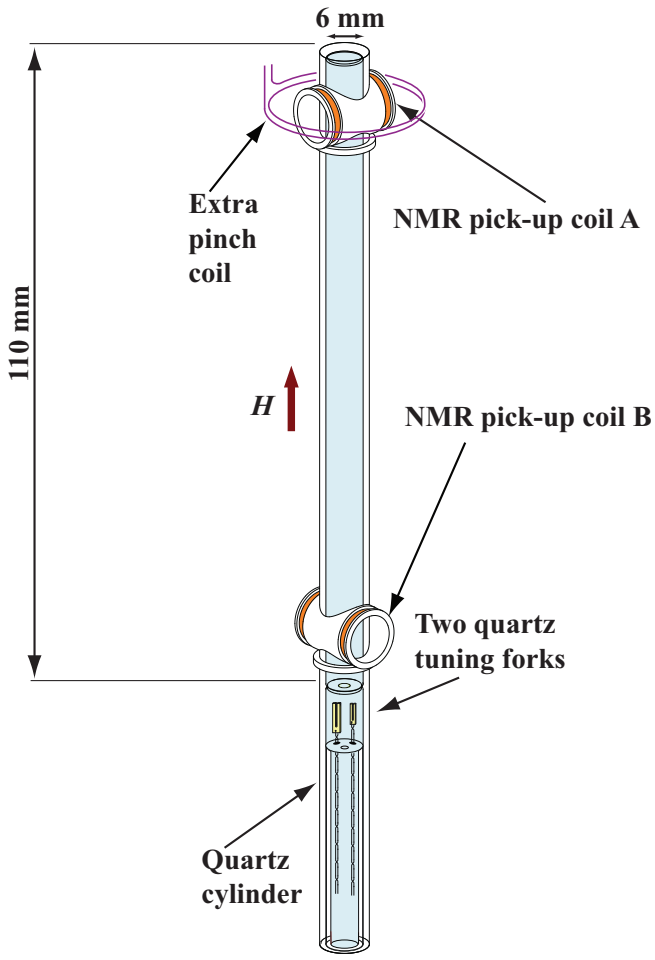

Figure 5.1: *Experimental setup for NMR measurements of ^{3}He.*

of the ^{3}He cylinder are used to measure the temperature of the sample [52]. An extra pinch coil around the NMR pick-up coil A is used to create a local minimum in the axially oriented magnetic field **H**. This provides the possibility to prepare and measure the condensate of magnons (See Sec. 7.4).

Both NMR detector coils are connected to their respective capacitor banks, which are thermally anchored to the mixing chamber situated above the nuclear stage. Above the mixing chamber, but inside the vacuum can isolating the 4.2 K liquid He bath and the low temperature parts, are situated the two preamplifiers, one for each spectrometer. They are tightly screwed on a gold plated copper support which is thermally anchored with copper conductors to the bath. Thus, the preamplifier boxes are fixed to the same ground potential and temperature as the cryostat surrounding them. All parasitic capacitances of the wires are also grounded to the preamplifier casing. The complete preamplifier assembly is seen

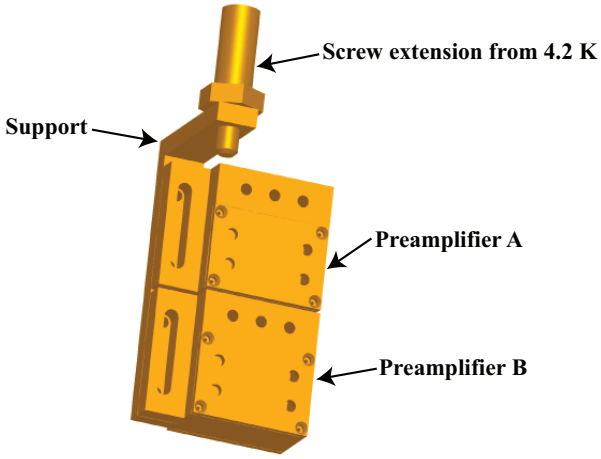

Figure 5.2: *Preamplifier assembly inside the cryostat.*

in Fig. 5.2.

5.1.1 Superconducting NMR magnet system

The sample cell and the NMR pick-up coils are inside the NMR-magnet system (Fig. 5.3 [4, 53]), which is suspended from the bottom of the mixing chamber. Because we use two spectrometers with different resonance frequencies, we need also two static NMR fields, H_A and H_B, which must not interfere with each other. The NMR magnet system consists of three concentric parts which slide into each other. The magnets are designed to operate at low currents to prevent quenches and to minimize the requirements on the power supplies. The superconducting wire is a $\varnothing$ 120 μm multifilament NbTi wire in CuNi matrix.

The innermost part contains the barrier or valve magnet. It is used to create and stabilize ^{3}He-A phase in the middle of the sample needed in dynamic vortex measurements. A field up to 0.5 T is needed for this purpose. The valve magnet is wound on a solenoid with an inner diameter of 17 mm. It has 21 layers, each with 90 turns. To minimize its influence on the homogeneity of the NMR fields, two counterwound end compensation coils are wound directly next to it from the same piece of wire. They squeeze the valve field in a narrow volume and thus minimize its effect on the homogeneity of the NMR fields. Their inner diameter is 20.8 mm and they consist of 3 layers each having 71 turns. There is an oxygen annealed high-conductivity copper cylinder inside each of the NMR magnets. This reduces the losses of the RF field H_{rf} in the magnet frame and maximizes the Q-factor.

The next part around the coil former of the valve magnet contains two NMR magnets, one for spectrometer A and one for spectrometer B. The NMR magnets

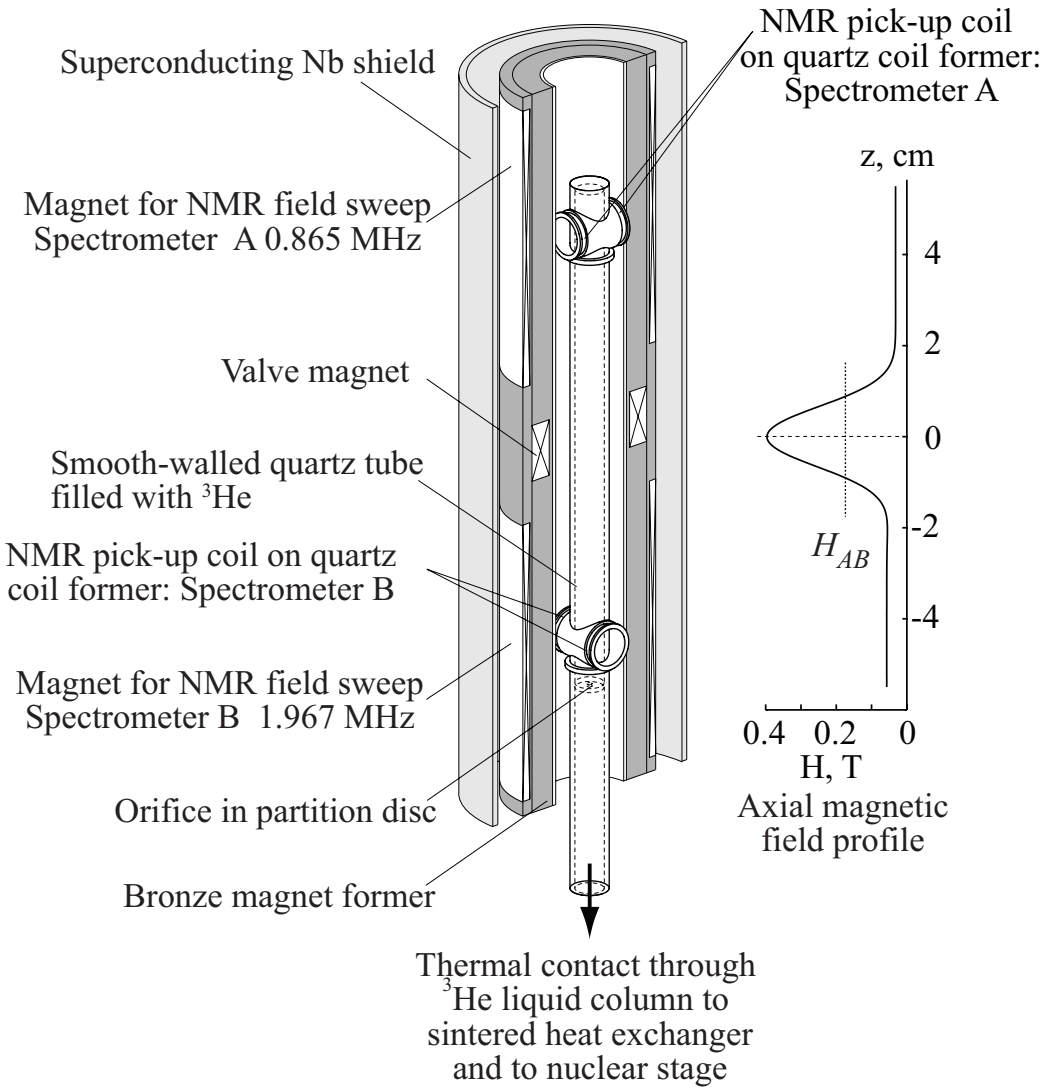

Figure 5.3: *NMR magnet system around the sample cylinder. On the right we see the field profile of the NMR magnets. H_{AB} refers to the field intensity at AB phase interface.*

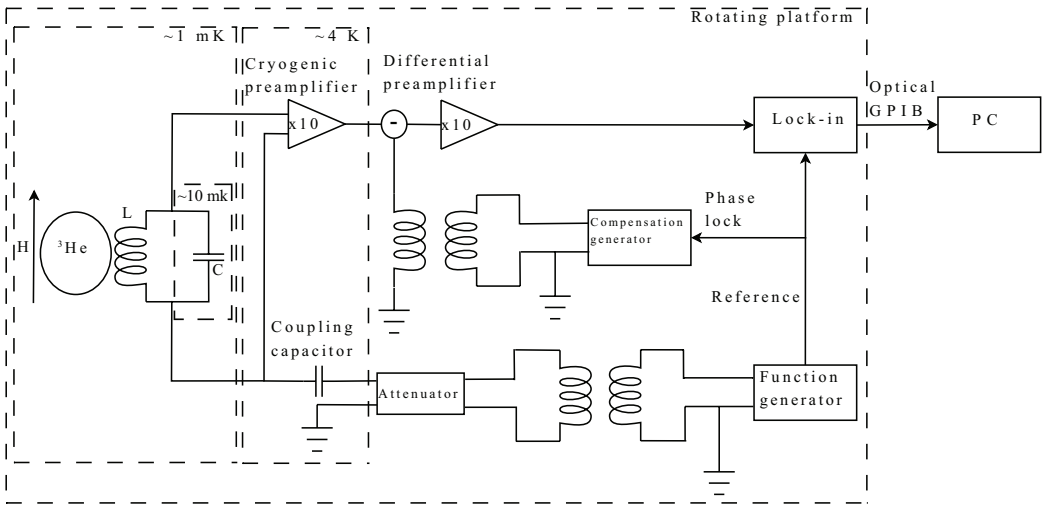

Figure 5.4: *Circuit diagram of the main devices in the NMR spectrometers.*

are end-compensated solenoids having an inner diameter of 28 mm. In addition they have a few counterwound turns on one side to null their field in the center of the other NMR magnet. Otherwise the NMR field sweeps would interfere with each other. The magnet coil in the top spectrometer has 2 layers of 450 turns and at both ends 2 extra layers of 27 turns. The counterwound coil, made from the same piece of wire, on the bottom of it has 12 turns. The NMR magnet in B spectrometer has 4 layers each with 450 turns and at both ends 2 extra layers of 45 turns. The counterwound coil on the top of it has 22 turns. To achieve the proper fields congruent with the Larmor frequencies presented in Table 4.1, we sweep the currents in the following way: between 2.7 and 2.8 A in the spectrometer A, and between 3.15 and 3.25 A in the spectrometer B. With these currents the strengths of the NMR fields are swept around $H_A \approx 26\,\mathrm{mT}$ and $H_B \approx 60\,\mathrm{mT}$.

The outermost part in the NMR magnet system is a superconducting Nb shield to improve the field homogeneity and to shield the NMR fields and the sample from external magnetic fields.

With the above configuration it has been observed that neither the valve field nor the demagnetization field has hardly any influence on the NMR measurement [4].

5.2 Measurement setup

The device configuration used in the measurements is presented in Fig. 5.4. The 50 mVpp sinusoidal excitation signal is derived from a HP 33120A function generator on the top carousel above the rotating cryostat. It is fed through the room

temperature isolation transformer and attenuator (usually 40, 60 or 80 dB) down to the preamplifier box at 4 K. From there the signal continues through the 1 pF coupling capacitor to the high Q LC resonance circuit which probes the ^{3}He sample at millikelvin temperatures. The voltage across the LC resonator changes depending on the magnitude of the magnetic field H and the state of the sample. The field H is swept and the resulting signal is amplified and isolated from the long transfer cable to room temperature by the cryogenic preamplifier (Sec. 3) at 4 K. After that the signal runs through a differential preamplifier (Stanford Research Systems SR560 or LeCroy DA1855A) at room temperature. It amplifies the signal and subtracts it from the compensation signal from a second phase-coherent generator (function generator HP 33120A). The compensation is used to subtract the strong excitation signal leaving only the weak NMR signal to be measured with the lock-in amplifier (Stanford Research Systems SR844). The compensation allows us to use the most sensitive settings of the lock-in amplifier which also makes it possible to measure the noise level properly. The output from the lock-in is read out via the GPIB bus through which also all other devices are controlled with the computer.

Chapter 6

Equipment tests

The purpose of the test program is to verify that the preamplifiers are working properly and to maximize the Q-factor of the resonance circuit and the signal to noise ratio (SNR) at the output of the preamps. During the test measurements the preamplifier and the resonance circuit are attached on a dipstick which is placed inside a helium storage dewar. The coil is firmly fixed inside a lead-covered container which provides protection from electromagnetic radiation and works as a diamagnetic shield at 4 K. All other devices are at room temperature outside the dewar in the same places where they will be in the actual measurements: on the rotating platforms of the cryostat. The device setup is similar to the one used in the real measurements (See Fig. 5.4) with the exception that the coil and the capacitor are also at 4 K and that there is no sample to be measured. We tested different coil and capacitor combinations together with different preamplifiers to investigate the behavior of the setup and to optimize the devices and values as much as possible before cooling down the cryostat and starting the actual measurements. Earlier test measurements, also at room temperature, can be found in Ref. [31]. In these tests we used a similar coil as in the actual measurements in spectrometer A (Sec. 4). We refer to this coil as the test coil in this chapter, while the "two-layer" coil refers to the actual coil to be installed into the cryostat. The capacitors were 680 pF and 1000 pF ATC series 100B porcelain high Q multilayer capacitors.

The Q-factor depends on multiple things in the device configuration, as described in Sec. 3. In addition to the components themselves, most remarkable is the choice of the V_{gs}-voltage, whereas V_{bias} has no significant effect either on the Q-factor or on the output amplitude A. The best Q-factor achieved was almost 40 000 (Fig. 6.1). In Fig. 6.2 we show the measured Q-factors as a function of the bias voltage V_{gs}. With some V_{exc}-V_{gs} combinations the response was nonlinear, so only the values from the pure Lorentzian response curves (Fig. 2.2) have been included. It is seen that the Q-factor changes significantly but no clear pattern is present. All changes and differences in the circuit affect the optimal value of

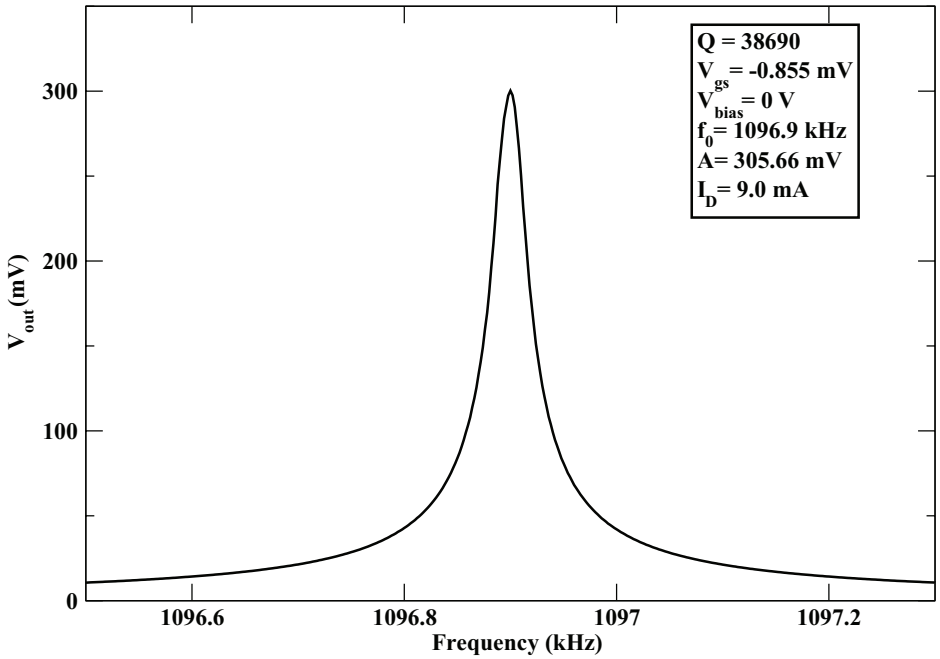

Figure 6.1: *One of the best Q-factors measured.*

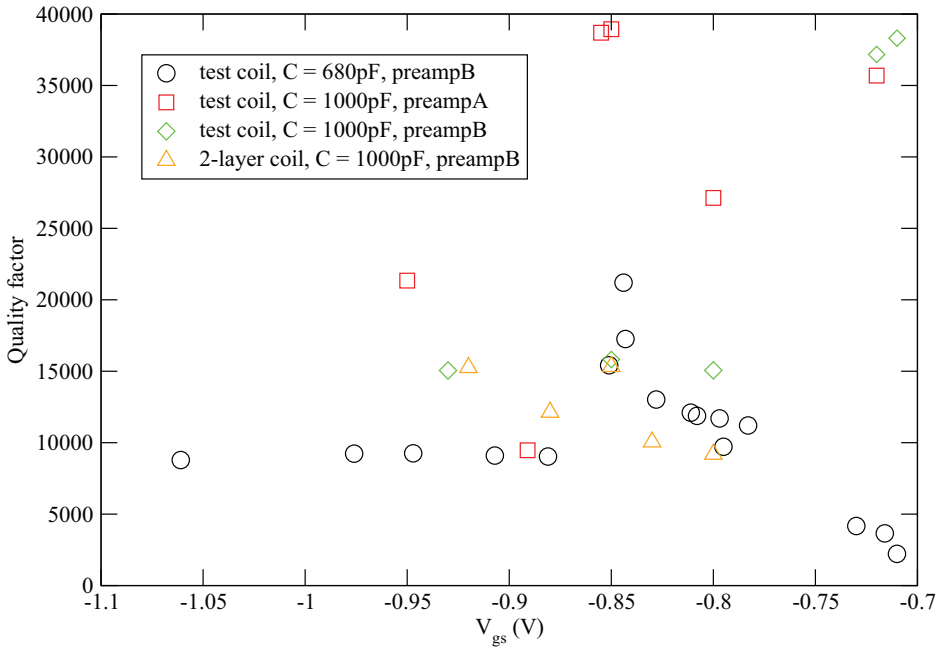

Figure 6.2: *Measured Q-factors plotted against the bias voltage V_{gs} from test measurements. PreampA and PreampB refer to the tested preamplifiers, which later were used for the top and bottom spectrometers, respectively.*

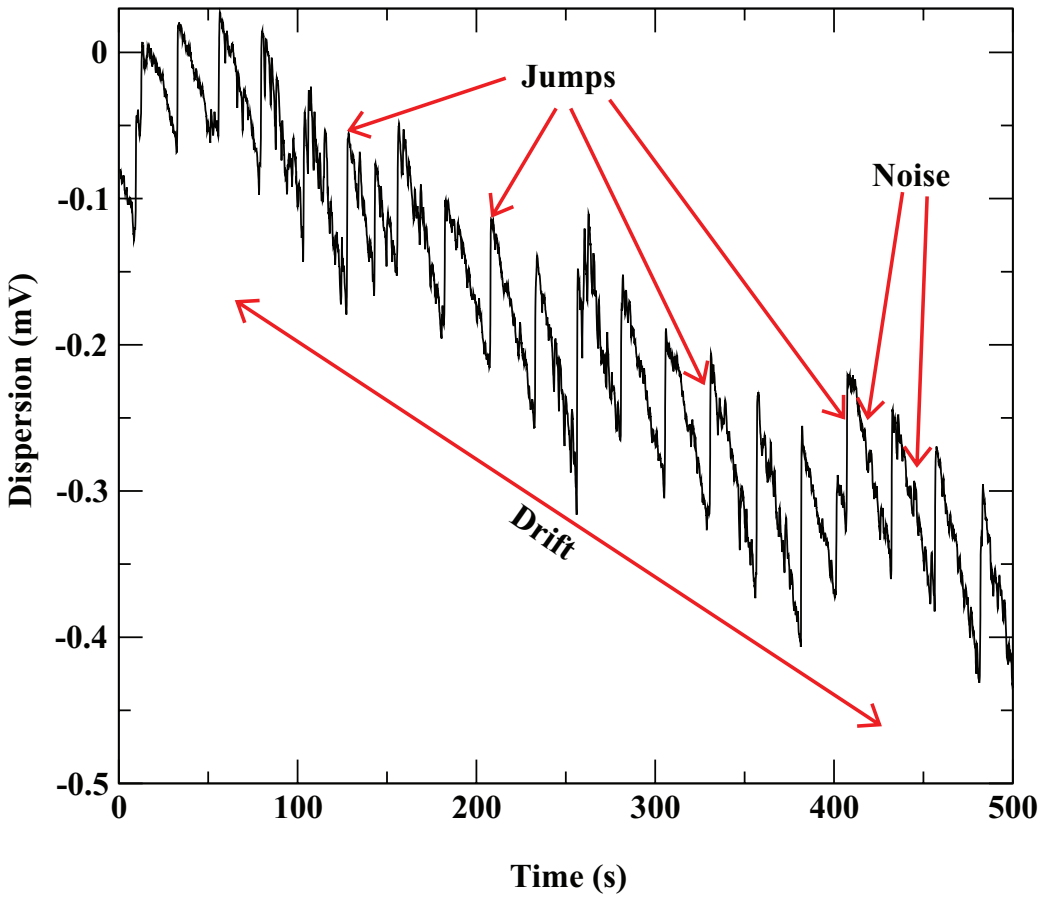

Figure 6.3: *An example of a dispersion signal showing the noise, the jumps, and the drift which occurred during the test measurements.*

V_{gs}. Thus it has to be optimized every time when cooling down before starting the measurements. The low temperature preamplifiers, for example, are not completely identical, so that results differ with different preamplifiers. Usually a value of V_{gs} between -0.8 and -0.9 V gave the best results. The amplification of the low-temperature circuitry (the resonator and the preamplifier together) depends on V_{gs} and the Q-factor (Eq. (2.27)). In our test measurements the output amplitude was measured to be between 50 and 400 mV with $V_{exc} = 0.5$ mVpp and amplification of 10 in the room temperature preamplifier. This gives a low temperature amplification between 20 and 160.

Noise was measured by adjusting the excitation frequency to the resonance value f_0 and by compensating the output signal, after which the resulting near-zero signal was recorded with a lock-in amplifier. Besides noise, strange jumps and drift were seen. Fig. 6.3 shows an example of the measured dispersion signal

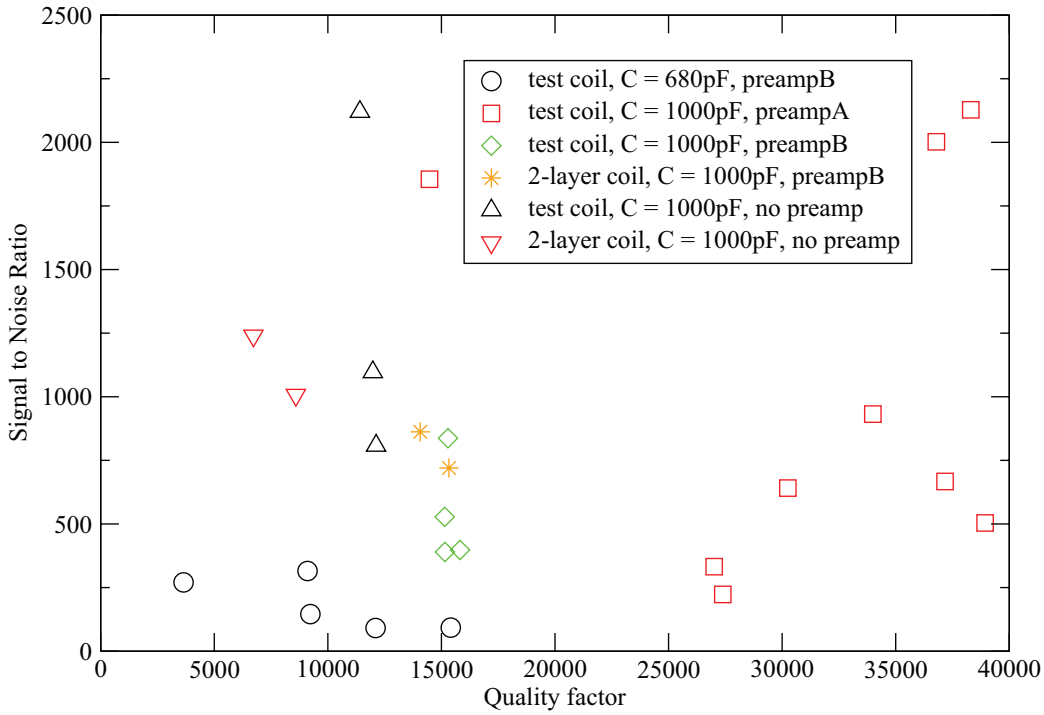

Figure 6.4: *Signal to noise ratio plotted against the measured Q-factor in the test measurements.*

at the lock-in amplifier output. The absorption signal was similar. The magnitude of the jumps depended on the V_{exc} and V_{gs} voltages but never exceeded 3 mV, which caused the jumps to blend into the noise with high V_{exc} and output amplitude A. The jumps mostly acted to compensate the drift. The drift itself was seen as a steady increase or decrease of the measured signal.

As a conclusion from the test runs, the drift was found to occur because of the unstable channel current I_D, which, in turn, caused f_0 and the output to drift. It takes a lot of time (hours in some cases) for the current to stabilize after adjusting the V_{gs} or V_{bias} voltages or after turning them on. The reason for this unstable operation is the temperature change of the FETs due to the change in the channel current. The bigger the change the longer it takes for the temperature (and the current) to stabilize. After taking this into account, and after keeping the voltage source always on and avoiding unnecessary voltage changes, the drift problem vanished. With our test setup the jumps never vanished at low excitation voltages. However, when the cryostat was closed and the actual measurements started, such jumps did not occur. The probable cause for the jumps in the test runs was improper shielding of the resonance circuit or wiring, a bad ground, a bad contact somewhere, or vibration of the wiring. Inside the cryostat the circuitry

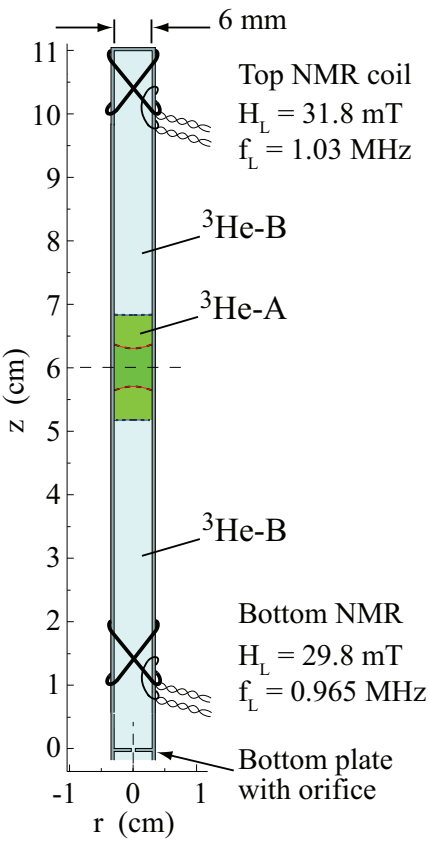

Figure 6.5: *The old experimental setup for NMR measurements of ^{3}He during the years 2005 to 2007. The difference to present setup is the absence of the coil formers and the cryogenic preamplifiers. Instead, the pick-up coils are wound directly on the quartz glass sample cylinder and the signal is read through a weak inductive coupling provided by a couple of turns of wire around the coil windings.*

is better shielded and less prone to vibrations due to better isolation and vibration-preventing design, e.g. semi-rigid cables, screwed connectors, and air bearings. Some of the connections throughout the circuitry were also remade before the actual measurements.

In spite of the drifts and the jumps we were able to measure the approximate base noise of the signal at different V_{exc} and V_{gs}. Step-by-step testing of all the devices was done to find the source of the noise. With only excitation generator, compensator, lock-in amplifier, room temperature amplifier, and the bias voltage source connected, the noise level was found to be below 1 μV. With the same settings, after connecting the resonance circuit, but not the low temperature preamplifier, the noise was 2-4 μV and the jumps emerged (10-70 μV). The signal

Table 6.1: *Preamplifier settings used during the ^{3}He measurements inside the cryostat at $T < 3\,mK$.*

Spectrometer	V_{gs} (V)	V_{bias} (V)	I_D (mA)	Q-factor
A	-0.956	0.005	2.3	10700
B	-0.965	0.006	2.15	3900

to noise ratio without the cryogenic preamplifier (SNR) was over 1000 and the maximum Q-factor about 12000. After adding the low temperature preamplifier into the circuit, both the noise and the jumps grew a little larger compared to the signal, and the SNR decreased. Fig. 6.4 shows the SNR as a function of the Q-factor from various measurements. The values are scattered, but it can be seen that a SNR between 500 and 1000 is common with our complete test setup. Based on the test measurements mentioned above, the main device contributing to the noise is the LC resonance circuit itself.

In the actual measurement environment inside the cryostat the superconducting coils are not so well isolated from the surroundings as they are in the test setup. Instead, they are tightly placed inside the NMR magnet system (Sec. 5.1.1), which brings the innermost annealed copper cylinder close to the coils. As a result, the Q-factors of the LC-resonators are remarkably reduced. Table 6.1 shows the bias voltages and measured drain currents and the Q-factors in our measurements at millikelvin temperatures. The bias voltages are kept constant during all the measurements, which prevents the fluctuation of the Q-factors and drain currents from one measurement to the next. Changes in temperature between the measurements are so small that they do not affect the Q-factors significantly. However, after doing a helium transfer or changing the excitation voltage, we have to wait for the preamplifier temperature to stabilize to avoid the drifting. For comparison, in the old setup (Fig. 6.5) the Q-factors for both spectrometers were about 6000. With even older setup before 2005, when we used solenoid-like RF coils and the earlier version of cryogenic preamplifiers, the Q-factor was 9300 on the top and 4800 on the bottom [4].

Chapter 7

^{3}He NMR-measurements

7.1 NMR response of normal liquid ^{3}He

Two examples of continuous-wave NMR responses from liquid ^{3}He, measured above the superfluid transition temperature (2.425 mK at our pressure, $p = 29$ bar), are shown in Figs. 7.1 and 7.2. Also the Lorentzian fits

$$y = A0 + \frac{A1}{(x - x_0)^2 + \gamma^2} \tag{7.1}$$

are shown. $A0$, $A1$, x_0 and γ are fitting parameters, from which we can get an estimate for the full width at half maximum (FWHM) of the response curve (FWHM $= 2\gamma$) [54]. The width is primarily determined by the inhomogeneity in the NMR polarizing magnetic field. The factors which play some role here are the NMR magnet itself, the transverse excitation field $H_{\rm rf}$, and the trapped flux in superconducting materials, particularly in the pick-up coil. The field inhomogeneities $\Delta H/H$ are calculated from the Lorentzian fits by dividing the FWHM with the peak position. The averaged inhomogeneities, calculated from 4 different peaks, are $\Delta H_A/H_A \approx 7.4 \cdot 10^{-4}$ and $\Delta H_B/H_B \approx 11.4 \cdot 10^{-4}$. The present inhomogeneities seem to be worse than the earlier ones with the same NMR magnet configuration and similar solenoid-like RF coils ($\Delta H_A/H_A \approx 3 \cdot 10^{-4}$ and $\Delta H_B/H_B \approx 7 \cdot 10^{-4}$ [4]). The reason for the difference could be that we have remade the RF pick-up coils to change the resonance frequencies. Now the number of layers and turns is different than before: earlier we had 27+27 at the top and 24+24 at the bottom, present numbers are shown in Table 4.1. The worse homogeneity seen by the bottom coil cannot be explained by these figures, however, since actually single layer coils (like the present coil in the bottom) used to provide the best homogeneity in the previous setups. So it could be that there is some problem with the bottom pick-up coil, as can also be concluded from its lower Q-factor.

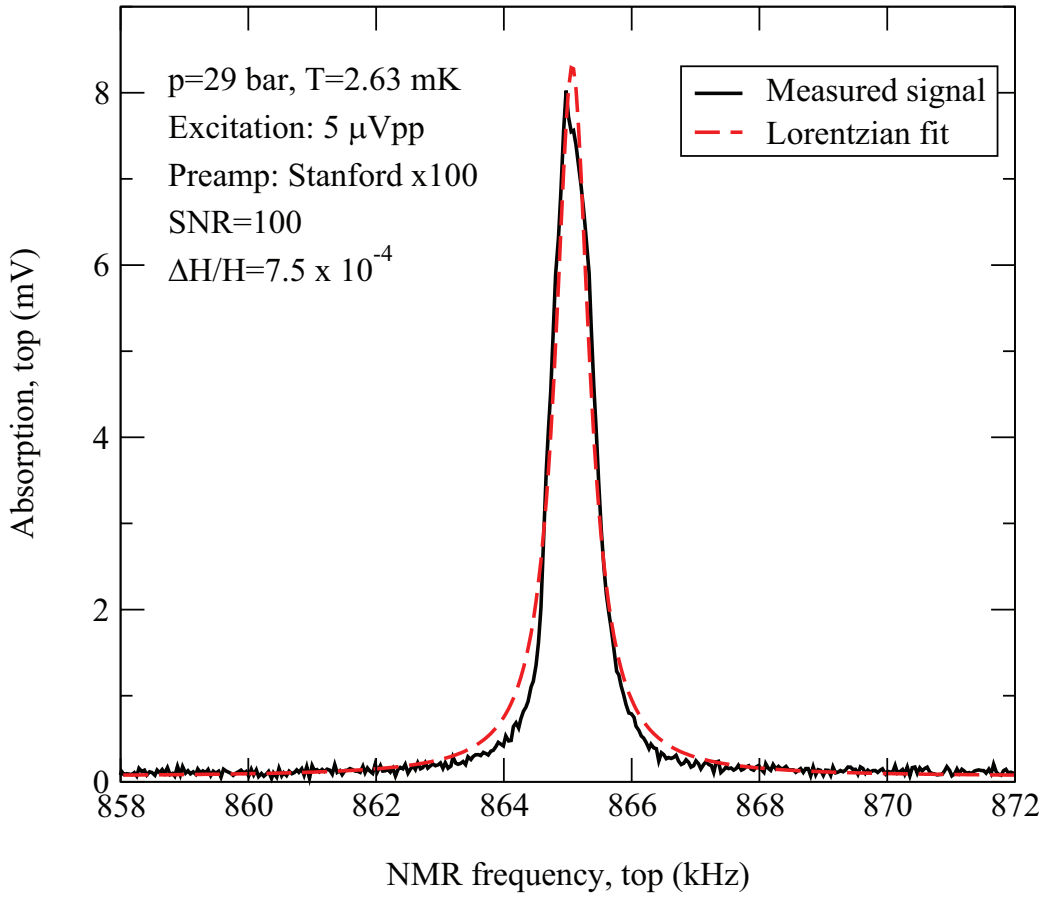

Figure 7.1: *NMR signal from normal liquid ^{3}He centered around a Larmor frequency $f_L = 0.865\,MHz$, as measured with the top spectrometer.*

The signal to noise ratio depends on the excitation amplitude. In Figs. 7.1 and 7.2 it is $5\,\mu$Vpp at the output of the attenuator feeding the excitation to the LC resonator (See Fig. 5.4) assuming $50\,\Omega$ load. With the more often used 0.5 mVpp we get $SNR_A \approx 5000$ and $SNR_B \approx 8000$. The reason for the difference between excitations is that the excitation-independent base noise from the devices is not changed as we change the excitation, so the noise does not increase at the same ratio with V_{exc}. The actual *SNR* values are better than the ones measured in tests because the cryostat is better isolated from the environment than our test setup. The old *SNR* values with the setup presented in Fig. 6.5 were $SNR_A \approx 3000$ and $SNR_B \approx 7000$, so we have maintained the same order of magnitude and even slightly improved. We measured the amplification of the low temperature circuitry at millikelvin temperatures to be $G_A \approx 90$ and $G_B \approx 20$. The amplification in the B spectrometer is smaller because of the worse Q-factor. Overall, the reason for

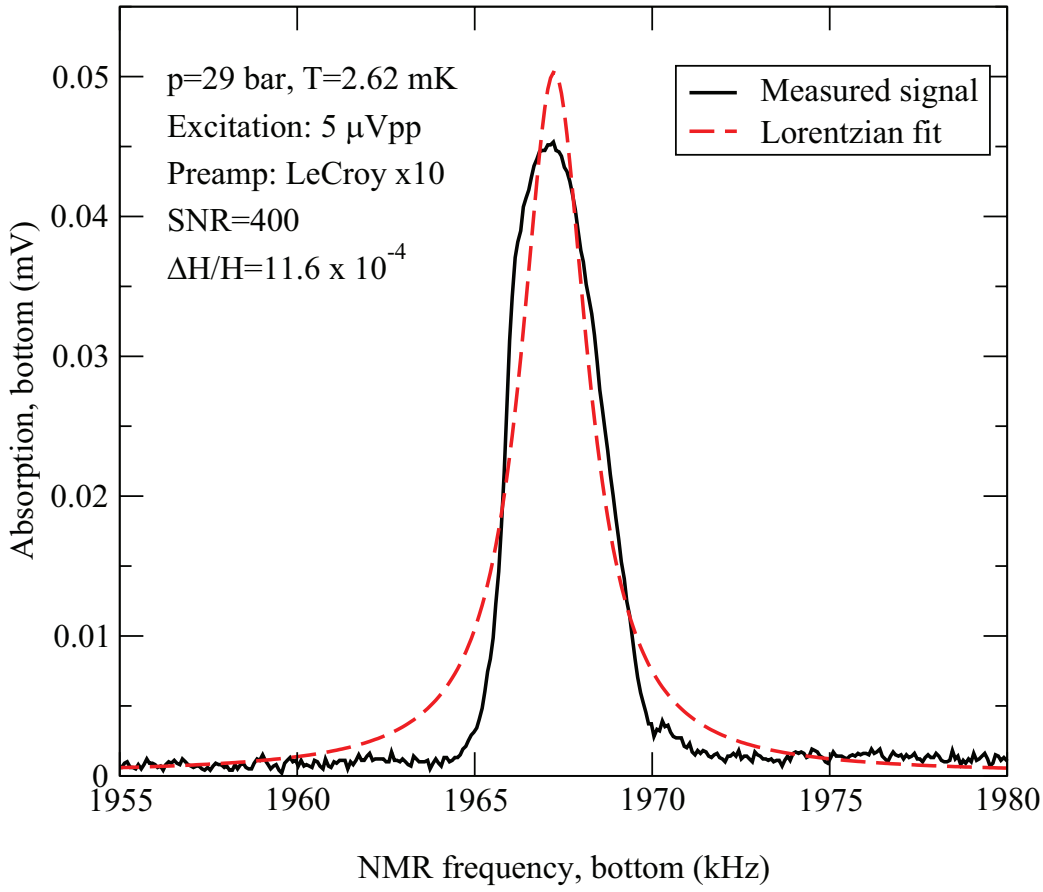

Figure 7.2: *NMR signal from normal liquid ^{3}He centered around a Larmor frequency $f_L = 1.967\,MHz$, as measured with the bottom spectrometer.*

Table 7.1: *Properties of spectrometers at $T < 3\,mK$.*

Spec.	NMR current (A)	H_L (mT)	H_L (mA)	$\frac{\Delta H}{H}\,(10^{-4})$	f_L (MHz)	*SNR*
A	2.7-2.8	2758.5	26	7.4	0.865	5000
B	3.15-3.25	3185.0	60	11.4	1.967	8000

the lower amplifications, compared to the test results, are the lower Q-factors.

Table 7.1 summarizes the important data for each spectrometer at low temperatures (around and below T_c). The values presented in the table are not sensitive to temperature changes at these temperatures, and no significant changes are seen between different measurements. For the Larmor field H_L we list the values determined from the location of the center of the Larmor peak in normal liquid measurements.

7.2 Fermi liquid saturation measurements

The longitudinal and transverse relaxation processes with relaxation times T_1 and T_2 are described in Sec. 2.2.2. Here we present the measurements performed on normal ^{3}He liquid to determine the spin-lattice relaxation time T_1. First we find the RF excitation voltage V_{exc} at which our sample does not saturate. Then we raise the excitation voltage to a high value and saturate the sample, while keeping H and H_{rf} constant. After the magnetization has stabilized, we lower V_{exc} rapidly to the non-saturating level determined earlier, and start sweeping the sample with rapid sweeps to produce a series of rising absorption peaks while the magnetization is recovering towards its equilibrium value corresponding to V_{exc} (method 1, Fig. 7.3). Another method (method 2, Fig. 7.4) is to measure the relaxation curve directly without sweeping after lowering V_{exc}. From the recorded peaks or relaxation curve as a function of time we can determine T_1. This cw-NMR procedure to obtain the relaxation time is called the saturation-recovery method [55].

In addition to the temperature, also the diffusion of atoms between the regions covered and not covered by the pick-up coils and surface effects on the walls affect the relaxation rate [56–59]. The larger the ratio of surface to volume the more dominant the wall effects are. In confined geometries, where surface effect dominate, T_1 is only hundreds of milliseconds, and surface roughness and impurities make relaxation even faster. Our sample contains also ^{4}He impurity on the level of 500 ppm. This results in that inside the experimental cell the outermost layer of our sample is actually ^{4}He because of its greater mass and stronger van der Waals interaction with quartz glass. The relaxation processes of ^{3}He on a ^{4}He film on Nuclepore polycarbonate substrate have been studied in Ref. [60], where T_1 was measured to be less than 1 s on that surface.

In our setup the amount of bulk liquid is large compared to the wall area making the surface effect less significant. Bulk T_1 should be on the scale of hundreds of seconds [61, 62]. Figure 7.5 shows one measured relaxation plot and the corresponding fit determined using Eq. (2.11). We obtain the spin-lattice relaxation time T_1 from the fit. The measured relaxation times with both methods for spectrometers A and B are presented in Table 7.2. The obtained values are in agreement with the previous studies. One possible source of error is that the V_{exc} values used was not really non-saturating and affected the results making T_1 look longer than it really is.

The difference between the spectrometers is due to the difference in the field H and the Larmor frequency ω_L. The classic treatment of spin relaxation gives approximately the following result which is essential to an understanding of ex-

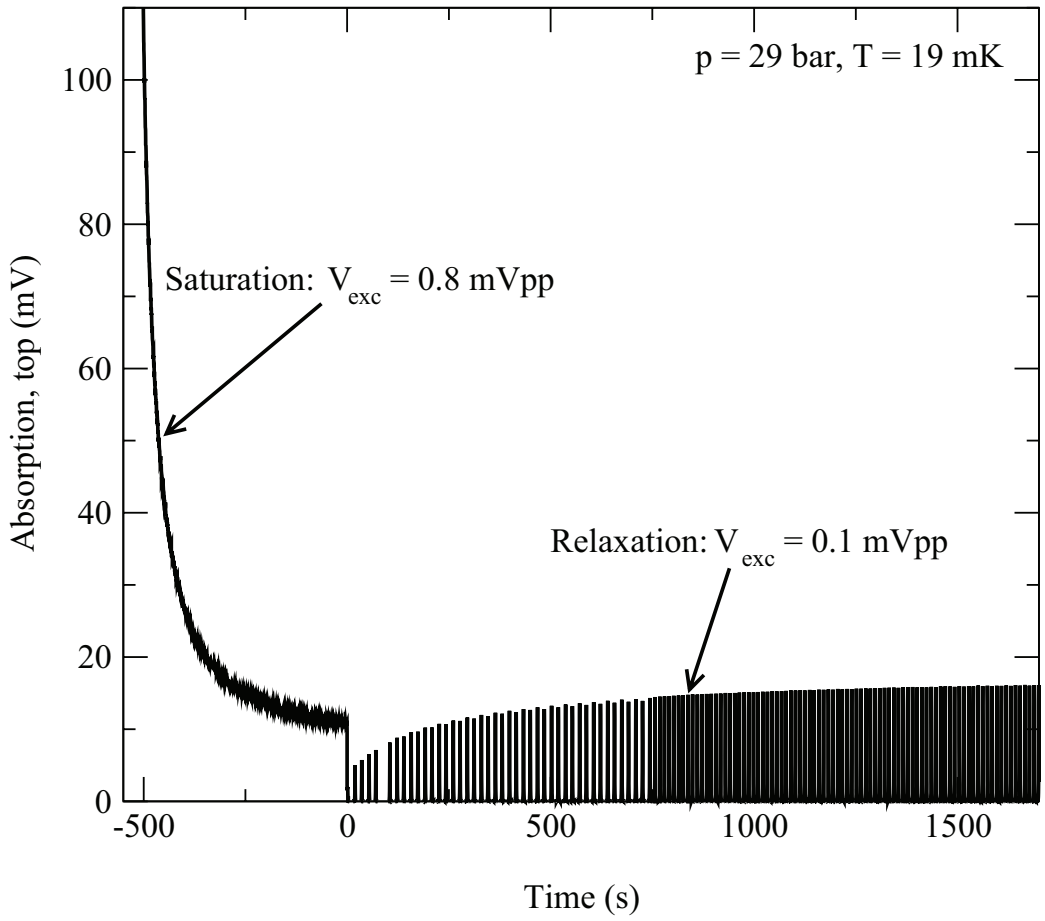

Figure 7.3: *Measurement to determine the spin-lattice relaxation time T_1. In this method a series of Larmor peaks is measured after V_{exc} is lowered to the measuring level.*

perimental bulk relaxation times [63]:

$$\frac{1}{T_1} \cong 0.3\gamma^2\hbar^2 b^{-6}\left(\frac{\tau_c}{1+\omega_L^2\tau_c^2}+\frac{2\tau_c}{1+4\omega_L^2\tau_c^2}\right), \tag{7.2}$$

where b is the average inter-spin distance and τ_c is the so called correlation time of the motion. In case of liquids with diffusion coefficient D the correlation time is defined as $\tau_c(r) = r^2/12D$ for atoms at distance r. The equation above gives a way to theoretically predict at least the order of magnitude for T_1 in ^{3}He as calculated in Ref. [61], the result being hundreds of seconds. For our purposes it gives an indication of the difference between the spectrometers: increasing ω_L increases T_1. However, usually $\omega_L\tau_c \ll 1$ and the effect of ω_L in Eq. (7.2) is not as large as detected. For full explanation we need to take into account the

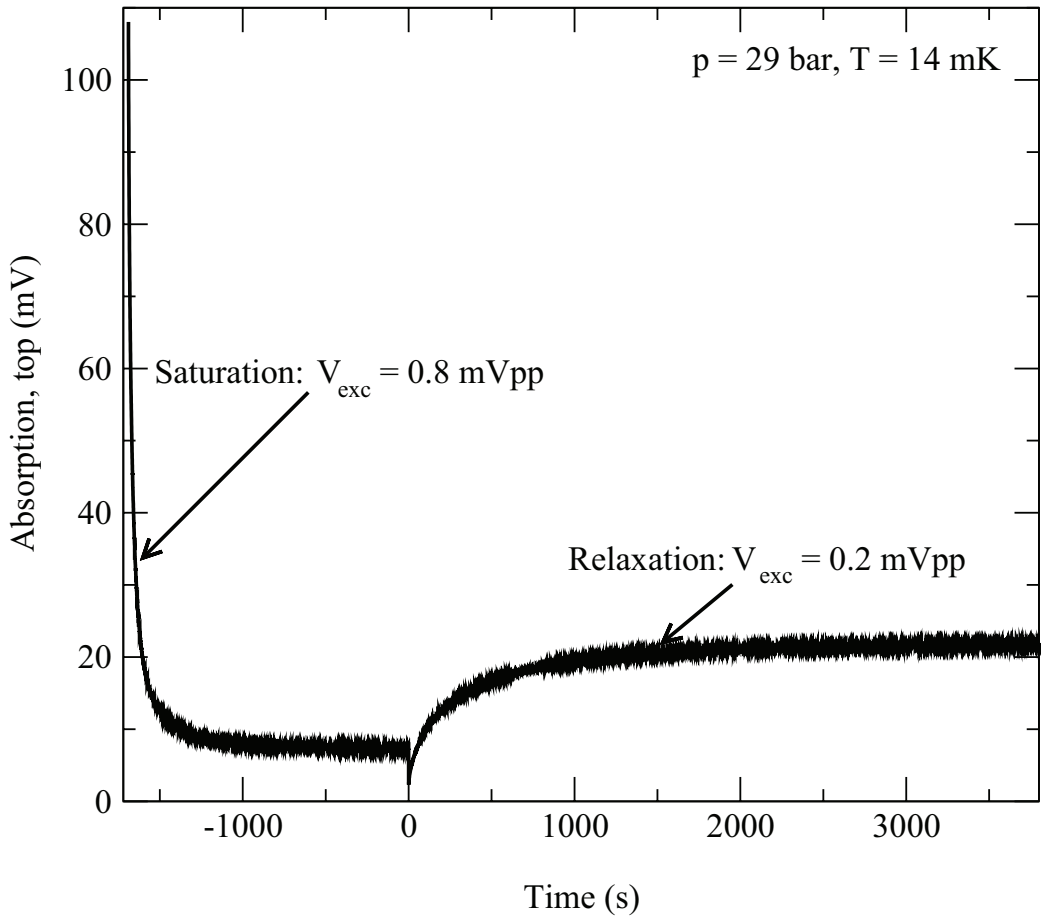

Figure 7.4: *Another method to measure the spin-lattice relaxation time. In this case V_{exc} is kept constant at the resonance frequency instead of sweeping it. The result is a continuous relaxation curve instead of multiple peaks.*

paramagnetic centers in the inner surface of our quartz glass sample cylinder. For example oxygen and the metal left in the glass work as so. At our polarizing magnetic field regime the centers have an effect to relaxation time through the magnetic coupling between the liquid and the walls. At low values of H the mutual magnetic interaction between the centers is significant increasing the coupling and decreasing T_1. At the level of mutual magnetic interaction there is a step-like connection between H and T_1 as increasing H saturates the paramagnetic centers reducing their effect on T_1. At high enough magnetic fields the paramagnetic centers are fully saturated and the magnetic coupling between the walls and the liquid is weak, i.e., the relaxation time is the highest.

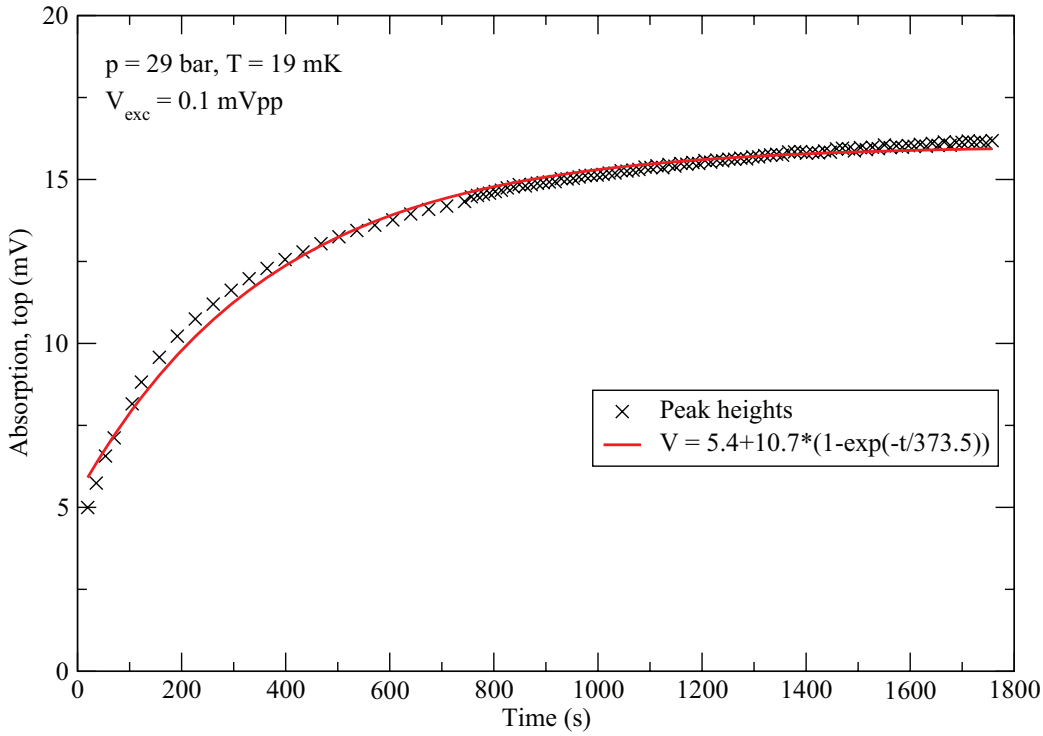

Figure 7.5: *Measured peak heights from Fig. 7.3 as a function of time. The spin-lattice relaxation time is determined from the exponential fit.*

Table 7.2: *Measured relaxation times from signal saturation.*

	Method 1			Method 2		
Spectrometer	T (mK)	V_{exc} (mVpp)	T_1 (s)	T (mK)	V_{exc} (mVpp)	T_1 (s)
A	19	0.1	370	14	0.2	450
B	19	0.25	730	14	0.5	700

7.3 NMR response of superfluid ^{3}He-B in vortex-free state

Theoretical background material on different textures and NMR responses of ^{3}He-B is presented in Sec. 2.3. Here we present more data measured in superfluid ^{3}He-B at different temperatures and rotation speeds with no vortices in the sample. All the data presented in this section is measured with the bottom spectrometer. The field profile in the top spectrometer is different and suitable for spin wave measurements. These results are presented in Sec. 7.4.

Figure 7.6 shows the measured spectra at different temperatures when no ro-

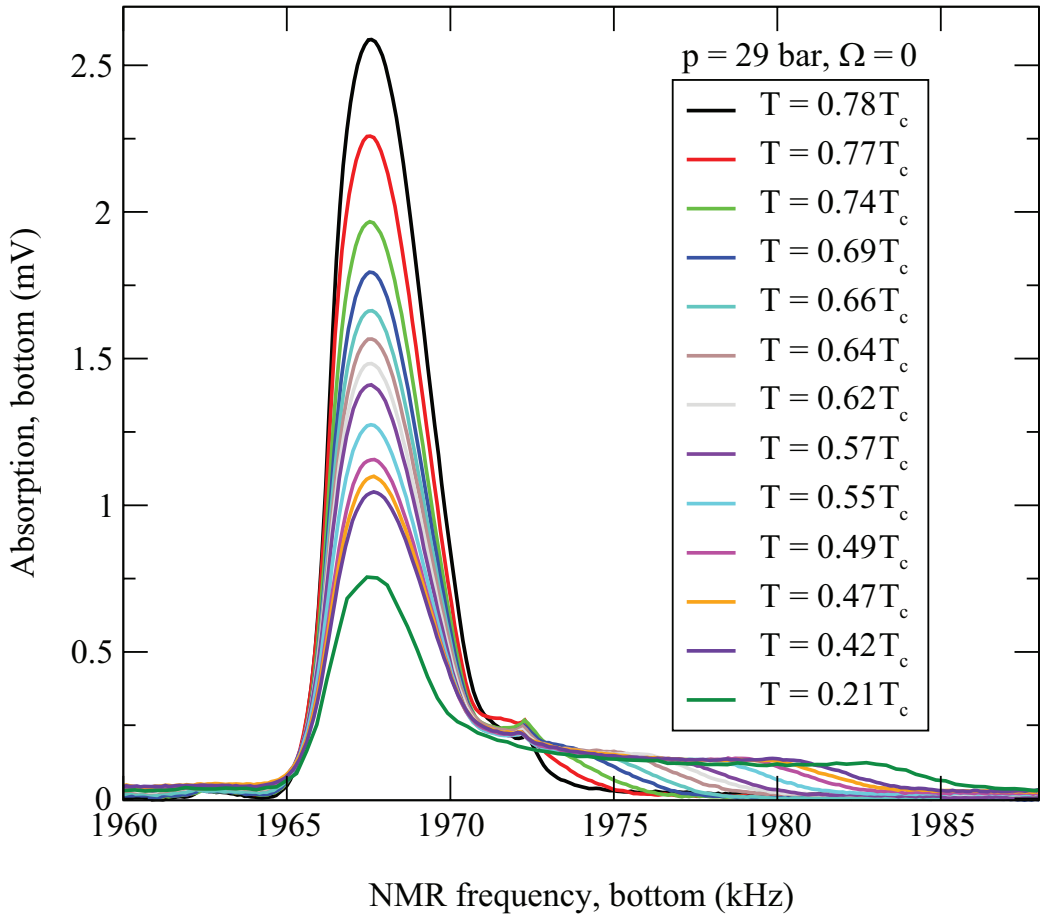

Figure 7.6: *NMR absorption spectra measured at different temperatures at zero rotation. With decreasing temperature the peak near the Larmor frequency is reduced and the tail grows longer. Kink to the right of the peak is caused by a textural inhomogeneity. The 0.21 T_c peak is measured in a different run where the distortion was not seen.*

tation is applied to the sample. According to Eq. (2.38), the resonance frequency is temperature dependent because the longitudinal resonance frequency $\Omega_B(p,T)$ depends on temperature. It increases with decreasing temperature, which makes the tail in the spectrum longer. This gives us the possibility to determine the temperature directly from the spectrum by extracting Ω_B from the end point of the tail, where $\beta \approx 63.4^\circ$ as described in Sec. 2.3.5. The temperatures listed in the figure are determined from the NMR-spectra (except the lowest temperature where Ω_B becomes more and more temperature independent). Temperatures calculated directly from the NMR-spectra tell accurately the actual temperature of the NMR sample at any given moment above 0.3 T_c. In all the other figures, how-

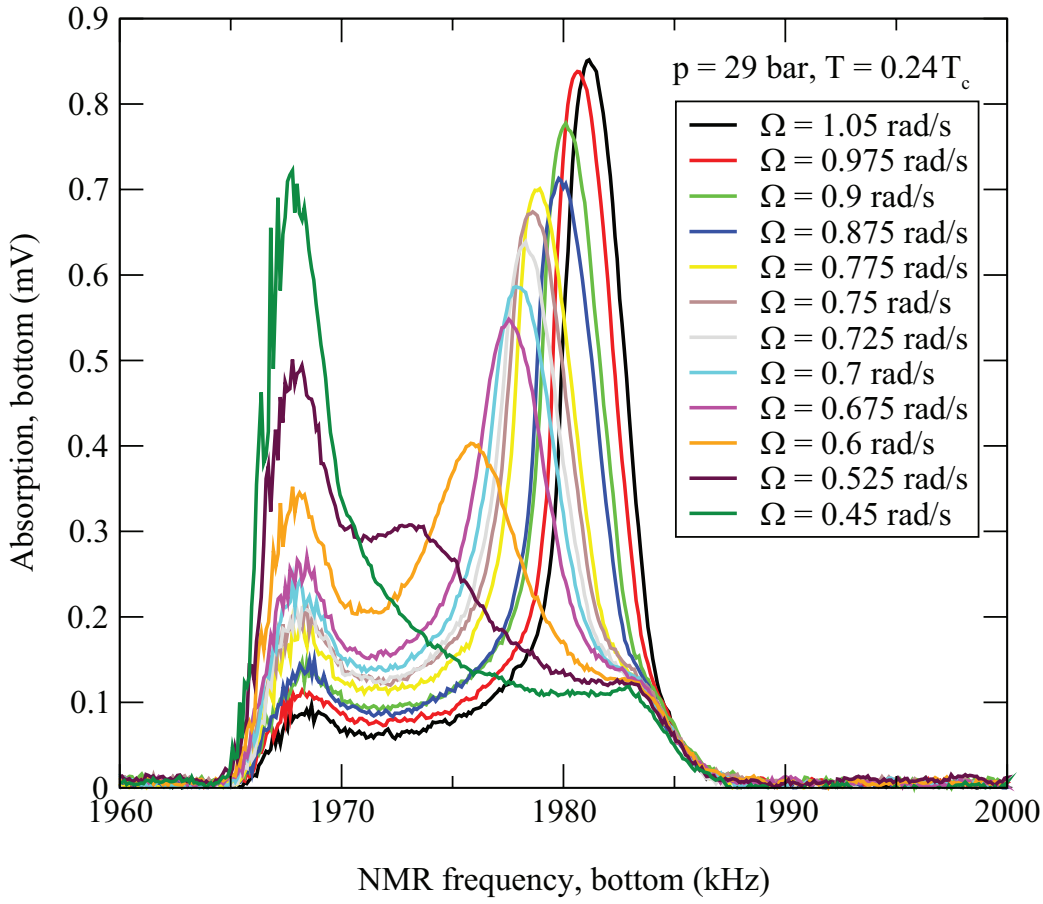

Figure 7.7: *NMR absorption spectra measured at constant temperature with rotation speed increasing from 0.45 to 1.05 rad/s. Simple flare-out texture is seen to transform into parted flare-out texture as the counterflow peak increases and the Larmor peak decreases.*

ever, the reported temperatures are either obtained from the calibrated ^{3}He melting curve thermometer (MCT) or from the quartz tuning fork readings, depending on whether we are above or below $0.3\,T_c$, respectively. At the lowest temperatures, where MCT does not work precisely anymore and Ω_B is saturated, the tuning fork is a sensitive and reliable thermometer, but owing to temperature differences between the various parts of the nuclear cooling stage at the lowest temperatures below about $0.35\,T_c$ calibration of the tuning fork reading is a delicate matter.

We mentioned textures in Sec. 2.3. Depending on temperature and rotation speed, different textures are seen. The textures in rotating vortex-free superfluid counterflow are called simple, parted, extended (or flare-in), and crowned flare-out textures [42]. The different counterflow textures are separated by textural phase

transitions of first or second order. The simple flare-out is seen at low rotation speeds ($\Omega < 0.45$ rad/s in Fig. 7.7). Its absorbtion spectrum consists of the peak near the Larmor frequency and a long tail (Fig. 7.6).

Increasing Ω gives a second-order transition to parted flare-out texture where the counterflow peak starts to emerge. With still increasing Ω the transition to the extended flare-out texture is observed. This transition is of first-order taking place in a hysteretic regime depending on whether rotation is accelerating or decelerating. In the extended flare-out texture a new peak, the 90 degrees peak ($\beta = 90^\circ$), is created as the maximum β-value extends to 116.6°, another wall- and flow-dominated free energy minimum of Eqs. (2.32) and (2.35). The 90° peak exists due to the fact that as β extends over 90°, $\sin^2\beta$ returns to the same values it had below $\beta = 90^\circ$, causing the absorption with these different β-values to occur at the same frequency. This is seen as a peak in the absorption spectra.

Finally, at high rotation speeds, we see the second-order transition to crowned flare-out texture. Then β equals mostly the wall- and flow-dominated value 63.4°, and the counterflow peak is the only peak in the absorbtion spectrum. In this regime the counterflow peak in the NMR spectrum can be used for temperature measurements. Ref. [42] presents detailed graphs showing the texture transformation dependencies on temperature and rotation speed.

Figure 7.7 presents spectra measured at $0.24\,T_c$ while gradually increasing the rotation speed up to 1.05 rad/s. The response seen shows two different textures: the simple and the parted flare-out textures. Figure 7.8 shows the situation where the rotation speed is gradually decreased after we have created the extended flare-out texture at $\Omega = 1.15$ rad/s and the 90° peak is found. The 90° peak is then seen in decreasing rotation in the hysteretic regime down to 0.7 rad/s. In Fig. 7.9 we see the texture transition as the temperature is decreased at constant rotation speed. As we also see, the counterflow peak height and frequency shift is really sensitive to temperature changes. Additional noise-like signal measured especially in the Larmor region in Figs. 7.7 and 7.8 is actually due to the spin-wave resonance discussed in Sec.7.4.

We see an additional surface peak not predicted by theory in Figs. 7.7 and 7.8. The probable explanation is the potential well created by the texture between $\beta = 90^\circ$ and the wall [64]. Spin-wave resonance can appear in this potential well causing a peak in the spectra similarly as described in Sec. 7.4.

Fig. 7.10 shows the peak heights from Figs. 7.6, 7.7 and 7.9 plotted against temperature and rotation speed. The difference observed is clear: peak heights change quite linearly with temperature, whereas the change with rotation speed looks exponential. The Larmor region peak height at $\Omega = 0.8$ rad/s decreases when the temperature is lowered, but increases when the 90° peak appears. Because of the textural transitions, the fits cannot be extrapolated beyond the measured regimes. For example, at $T = 0.24\,T_c$ the counterflow peak does not exist

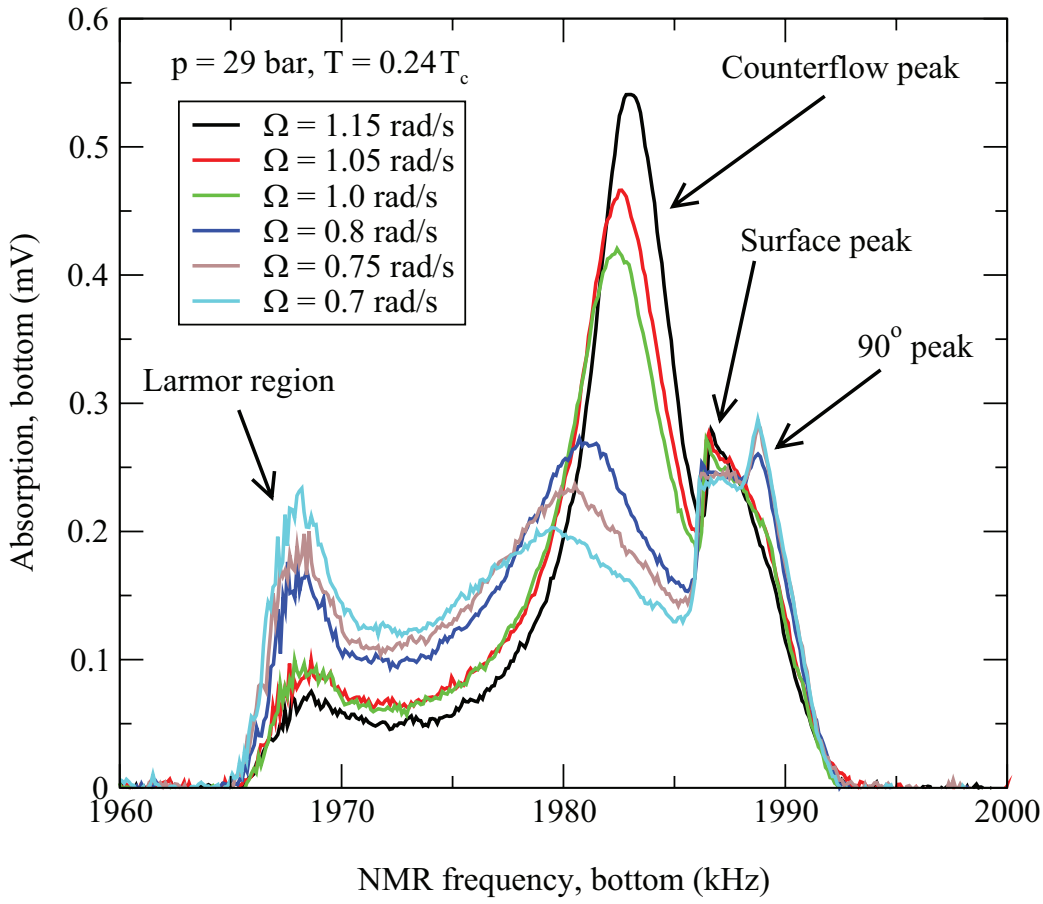

Figure 7.8: *NMR absorption spectra measured when the rotation speed is decreased. In this case the extended flare-out texture is seen, and the* 90° *peak and the surface peak are recognizable.*

anymore below $\Omega \approx 0.5$ rad/s.

The presence of the vortex bundle in the sample modifies the texture by affecting the free-energy terms related to counterflow and vortices (Eqs. (2.32) and (2.37)). Compared to the vortex free sample, the counterflow peak is reduced and the Larmor region peak increased as the number of vortices increases (as opposed to increasing the rotation speed). We can deduce the number of vortices in the sample from the counterflow peak height by comparing the vortex free peak heights at different rotation speeds to the ones with vortices. In order to perform measurements on vortices and their dynamics at certain constant temperature, the counterflow peak height must first be calibrated to different rotation speeds at that very same temperature. Because of the high temperature sensitivity, textural defects and instabilities, or uncontrolled number of vortices, we have to redo the

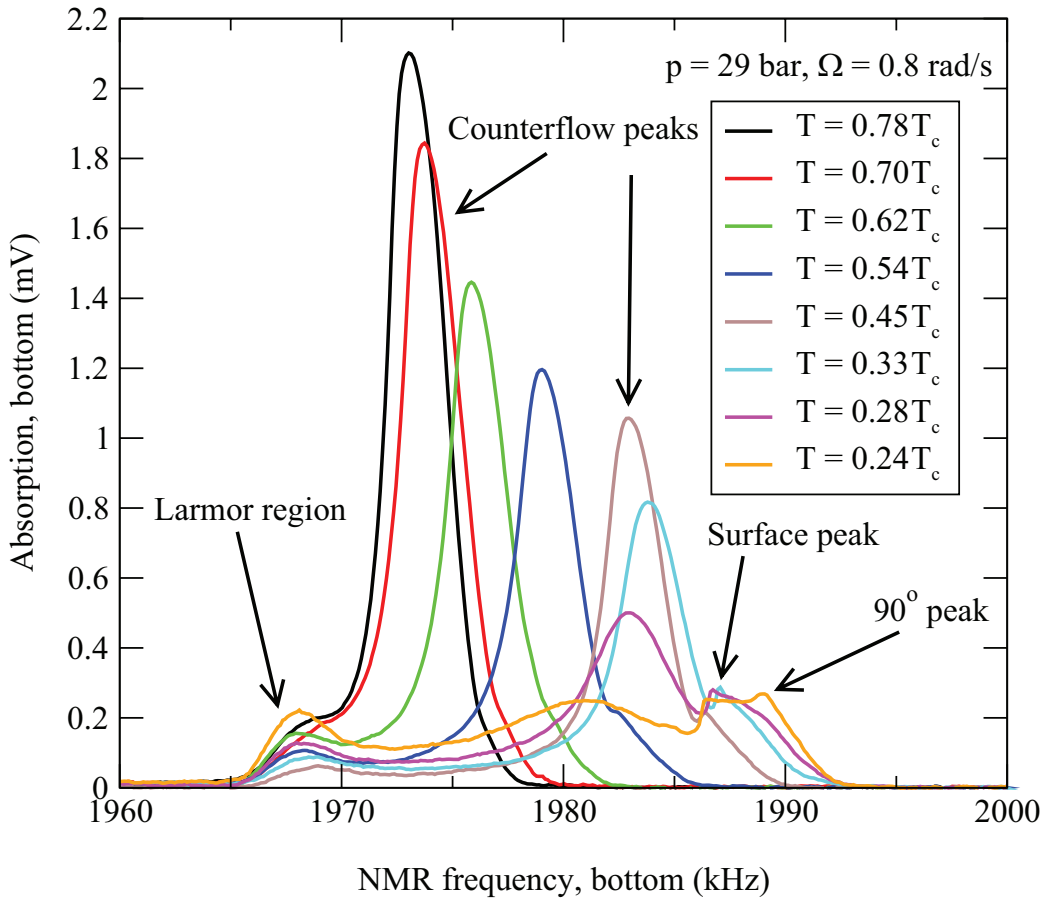

Figure 7.9: *NMR absorption spectra measured at constant rotation speed of 0.8 rad/s as the temperature is decreasing. Between 0.3 and 0.4 T_c we see the 90° peak forming. This is the texture transition from the parted to the extended flare-out texture.*

calibration again in the beginning of every run. Counterflow peak calibration in our current measurements has been described in Ref. [65].

7.4 Spin-wave results

7.4.1 Theory

In the local oscillator model (Eq. (2.38)) the shape of the absorption spectrum in ^{3}He-B is determined by the local value of β. In the previous sections a number of different line shapes are shown. The effect of temperature and rotation on β and, furthermore, on $\hat{\mathbf{n}}$ and the flare-out texture is clear and the local oscilla-

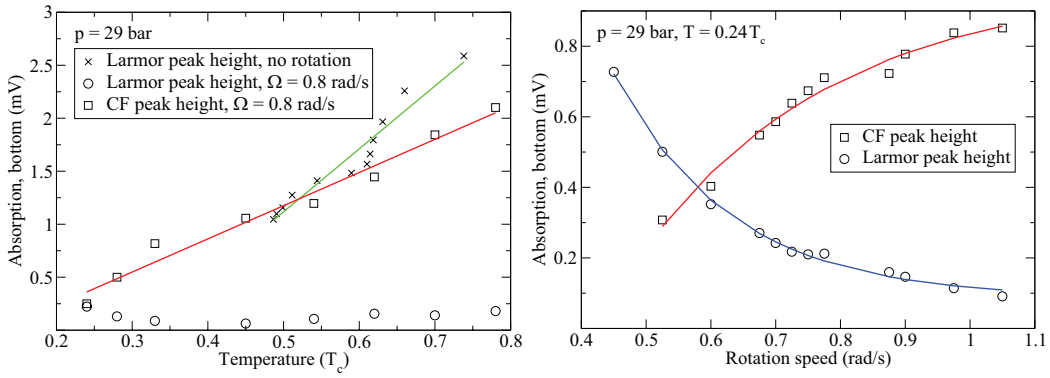

Figure 7.10: *On the left panel we see the almost linear temperature dependence of the Larmor region peak and the counterflow peak heights at two different rotation velocities. The right panel shows the exponential-like dependencies of the Larmor region and the CF peak heights as a function of rotation speed at constant temperature.*

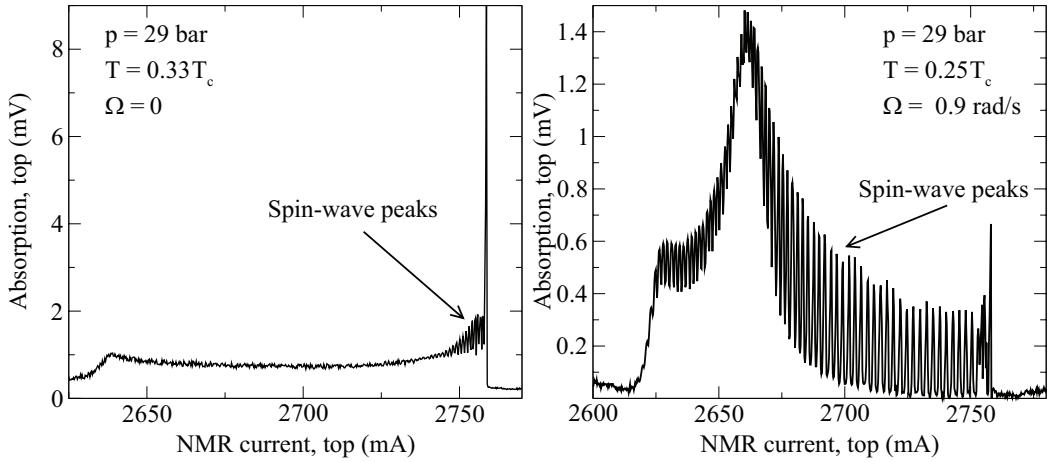

Figure 7.11: *Two absorption spectra measured with the top spectrometer. Satellite peaks caused by the spin-wave modes are seen on the spectra. At these temperatures the background shape of the spectrum is still determined by the local oscillator model, so that the peak near the Larmor edge and the counterflow peak are still recognizable.*

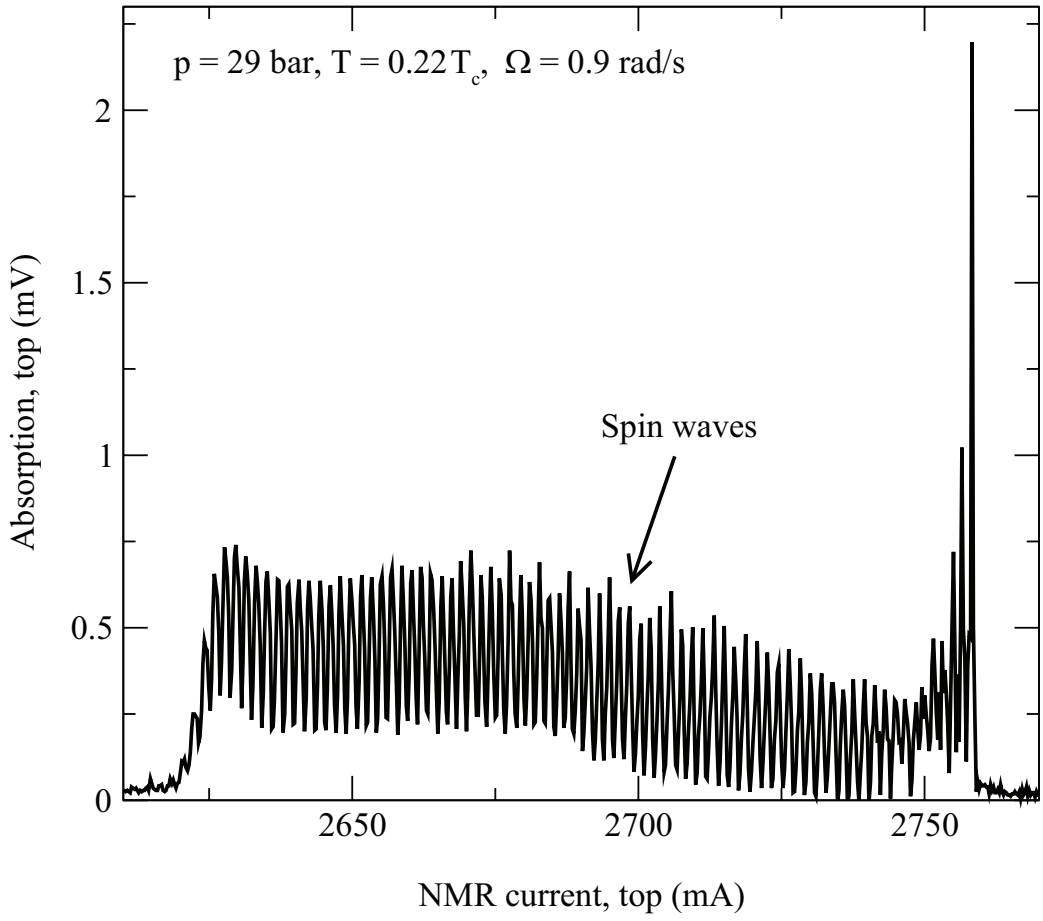

Figure 7.12: *Spectrum dominated by the spin-wave resonance peaks. The rotation speed is not affecting the general background shape of the spectrum anymore at this temperature, but only the satellite peaks are seen throughout it.*

tor model seems to be working. However, while the general shape of the NMR spectrum obeys the local oscillator model, it is possible to see multiple additional absorption peaks emerging at the lowest temperatures (Fig. 7.11). At low enough temperatures (e.g. $0.22\,T_c$) these satellite peaks start to dominate the spectrum, and the low-lying general shape of the spectrum is no more recognizable, regardless of the rotation speed (Fig. 7.12). The existence of these satellite peaks can be explained as spin-wave modes arising from an almost harmonic potential well formed by the $\hat{\mathbf{n}}$ texture. An accurate treatment of Leggett's general equations of spin dynamics is required for theoretical interpretation [34, 66]. In particular, we need to allow for global, coherent spin precession which, in the high field limit, can be reduced to a single equation describing the motion of the transverse spin

operator $S_+ = S_x + iS_y$ [67],

$$\left(-\frac{48}{65}\xi_D^2\nabla^2 + \sin^2\beta(r)\right)S_+ = ES_+, \tag{7.3}$$

where ξ_D is the dipolar healing length in ^{3}He-B. This equation is a Schrödinger-like equation, with $\sin^2\beta(r)$ acting as the potential term. The units for the eigenvalues E can be written in terms of a relative frequency shift

$$E = \frac{2f_L}{f_B^2}(f - f_L), \tag{7.4}$$

Near the center of the cylinder the inclination of $\hat{\mathbf{n}}$ from the external field direction remains small. In this part of the texture $\sin\beta(r) \approx \beta_1 r$ and Eq. (7.3) reduces to that of a harmonic oscillator. The slope of $\beta(r)$ in the flare-out texture is marked as β_1. The eigenvalues of harmonic oscillator from Eq. (7.3) are given by the equally spaced harmonic spectrum

$$E_n = 2(n+1)\left(\frac{48}{65}\right)^{(1/2)}\xi_D\beta_1 \tag{7.5}$$

with $n = 0, 2, 4, ...$, because in uniform polarizing and RF fields only even harmonics are excited. Thus, by combining the two equations above, the theory predicts equally spaced frequencies for the spin wave modes

$$f_n - f_L = f_L^{-1}(f_B^2)(n+1)\left(\frac{48}{65}\right)^{(1/2)}\xi_D\beta_1. \tag{7.6}$$

The above harmonic approximation is expected to be sufficient for the experimentally observed spin-wave peaks as long as β remains small. More generally, however, Eq. (7.3) should be solved with the appropriate potential well $\sin^2\beta(r)$.

7.4.2 Spin-wave analysis

In our top spectrometer (A) we see the spin waves prominently in the measured spectra. In the bottom spectrometer (B) some spin waves are seen in the spectra, but the amplitudes of the peaks are smaller and the spin waves are in limited frequency ranges close to the maximum of the peak in the Larmor region or that from the azimuthal vortex-free counterflow (e.g. Larmor frequency region in Fig. 7.7). The reason for this is the higher static NMR field in spectrometer B. This indicates higher Larmor frequency and thus, according to Eq. (2.38), makes the relative width of the spectrum narrower and spin waves more tightly spaced.

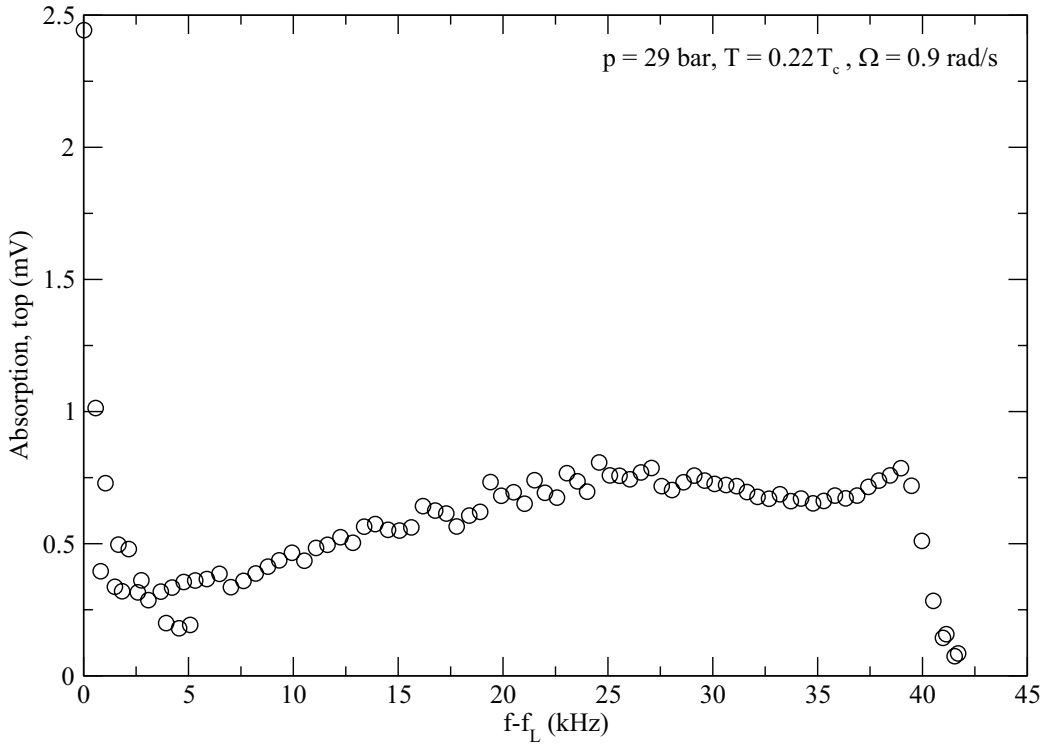

Figure 7.13: *Frequency shifts and amplitudes of the spin wave peaks shown in Fig. 7.12, based on quadratic fits to individual absorption maxima. The low amplitude peaks near the Larmor end are misreadings caused by noise.*

To see spin waves well in a narrow high-field spectrum we would also need better field homogeneity $\Delta H/H$. By contrast, the maximum number of spin-wave peaks in the A-spectrum is much larger (almost 100) than previously measured in Refs. [7, 67] (only a couple of peaks) because of the much lower temperatures.

For analysis to identify individual absorption maxima we make a quadratic fit to each spin-wave peak (for the baseline corrected data). Based on these fits, Fig. 7.13 shows the peak locations and amplitudes for the spectrum shown in Fig. 7.12. Due to our sweep resolution, each peak is determined by just three to seven points. Near the main peak (the highest peak) the spin wave peaks are more closely spaced, narrower, and higher than in the rest of the spectrum increasing the probability of falsely detected peak locations in this region. This makes the data look noisy near the main peak. The number of false readings caused by the actual noise in the signal can be reduced by controlling the width of the accepted peaks. After this, the most evident false peaks still left are removed and the corresponding frequency spacings are recalculated.

For further analysis we calculate the frequency difference between adjacent

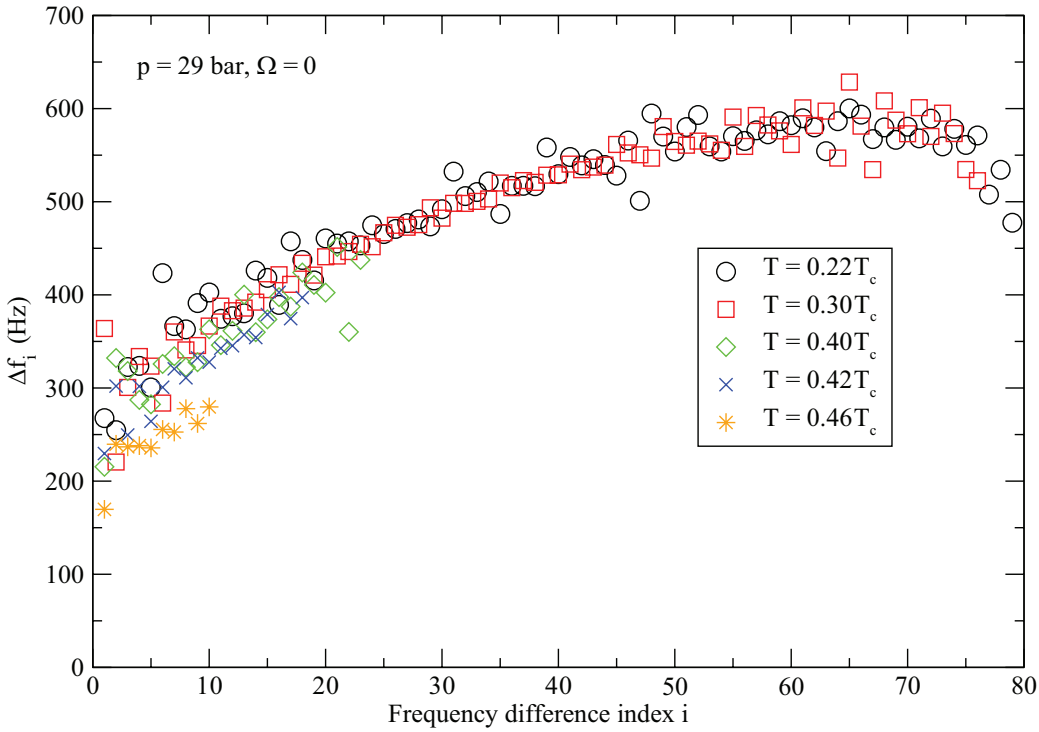

Figure 7.14: *Spin wave peak spacing along the spectrum at different temperatures. At higher temperatures the number of detected peaks is small.*

peaks along the spectrum. Fig. 7.14 shows this data at different temperatures. We denote the frequency between the main peak and the first satellite by Δf_1, the frequency between the first and the second satellites by Δf_2 and so on. We see that the number of detected peaks in the spectrum greatly depends on temperature. At $T = 0.22\,T_c$ and $T = 0.3\,T_c$ we see about 80 peaks but at higher temperatures the number is significantly smaller, e.g., at $T = 0.46\,T_c$ the peak number is only about 10. This number at higher temperatures is consistent with earlier findings [7]. Temperature has an effect on the spacing through the longitudinal resonance frequency f_B: at higher temperatures f_B is smaller and thus the spacing is smaller compared to low temperatures (Eq. (7.6)). We also see that the frequency spacing increases as we move from the Larmor region (the center of the cylinder) closer to the walls. This is expected from Eq. (7.6): in the simple flare-out texture near the middle of the cylinder β_1 is small and closer to the walls β raises faster towards 63.4° [42]. And where the harmonic approximation does not apply we can see directly from Eq. (7.3) that increasing β increases E and thus the spacing between peaks.

The frequency spacing between the first few peaks in the center of the cylinder

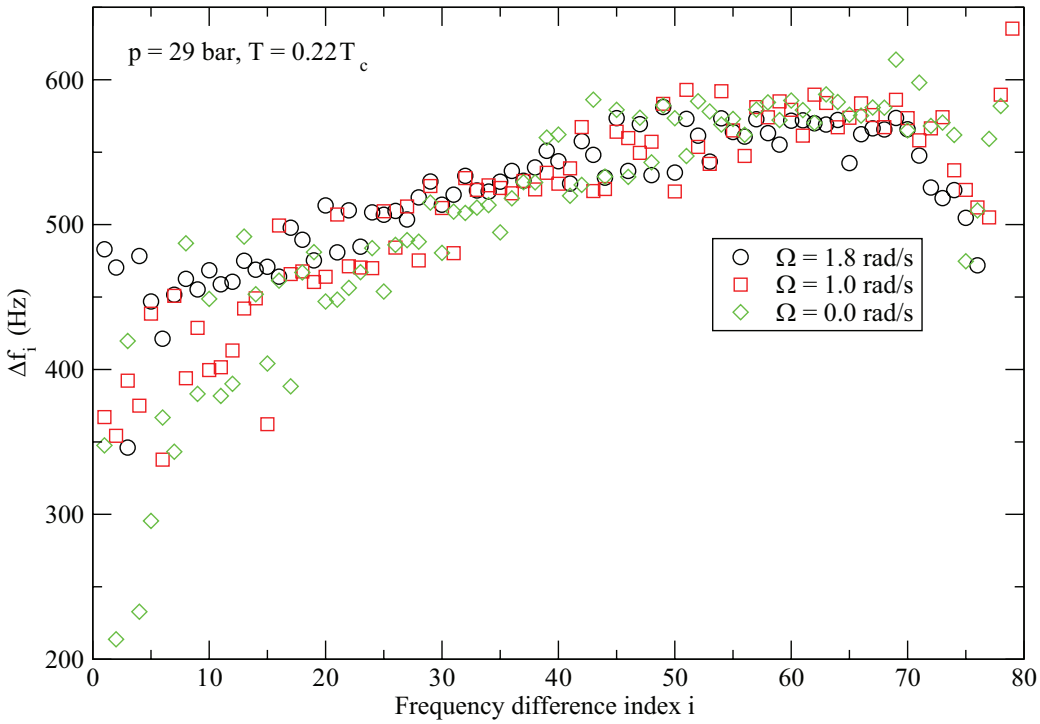

Figure 7.15: *Spin wave peak spacing along the spectrum at different rotation velocities at* $T = 0.22\,T_c$.

depends strongly on rotation velocity due to the changing texture [7, 67]. At higher velocities the peaks are further apart from each other as the slope of β is larger. Fig. 7.15 shows peak spacings for different Ω at the temperature $0.22\,T_c$. Although especially the region of the first few peaks is pretty noisy, and no definite conclusions can be drawn, our data shows a similar relation between Ω and the first peak spacings as detected earlier. It can be also seen that after some number of peaks the difference between different Ω is no more present, and the peak spacings with every rotation velocity seem to settle at the same level. Again, the explanation is found from the behavior of β with different Ω: at high rotation velocities (and with no rotation) β eventually settles to a constant value of 63.4° and the higher the rotation velocity the closer to the middle of the cylinder this happens (crowned flare-out texture).

The magnetic healing length ξ_H (Eq. (2.34)) has a significant effect on the β-inclination increasing the number of parameters affecting the above discussion. These relations have been studied in Ref. [67].

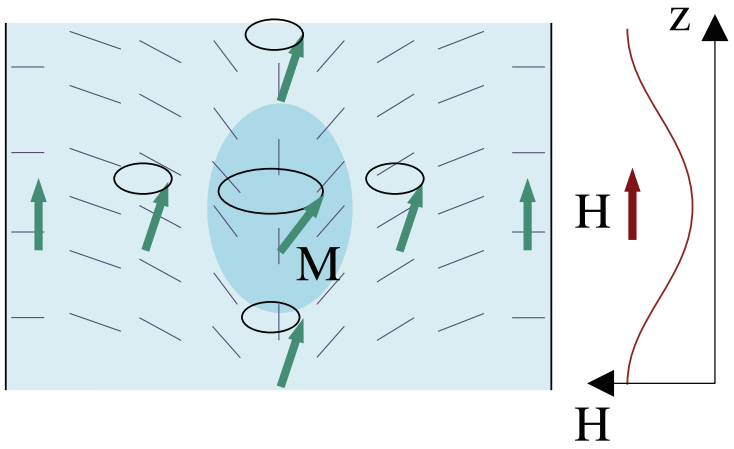

Figure 7.16: *Trapping potential formed by the flare-out texture of the orbital angular momentum* **L** *(blue lines) and by the minimum of the vertical magnetic field* **H**. **M** *is the magnetization which precesses coherently within the condensate droplet (dark blue).*

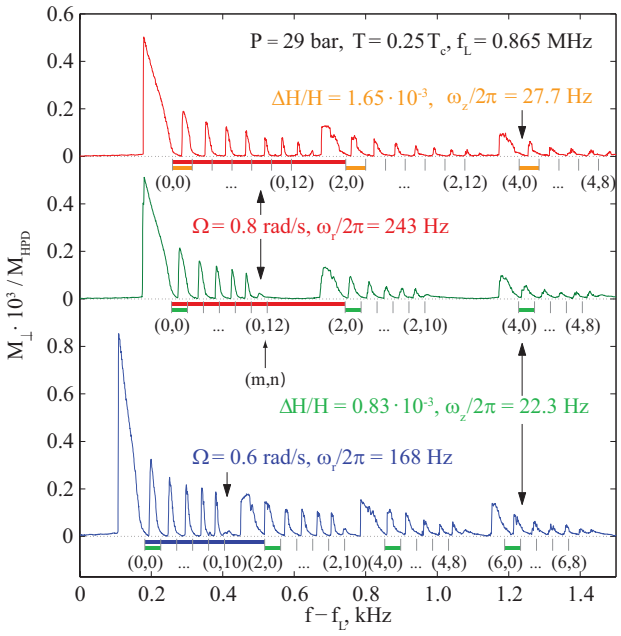

Figure 7.17: *The effect of rotation speed and the depth of the field minimum on the spin-wave peak locations.*

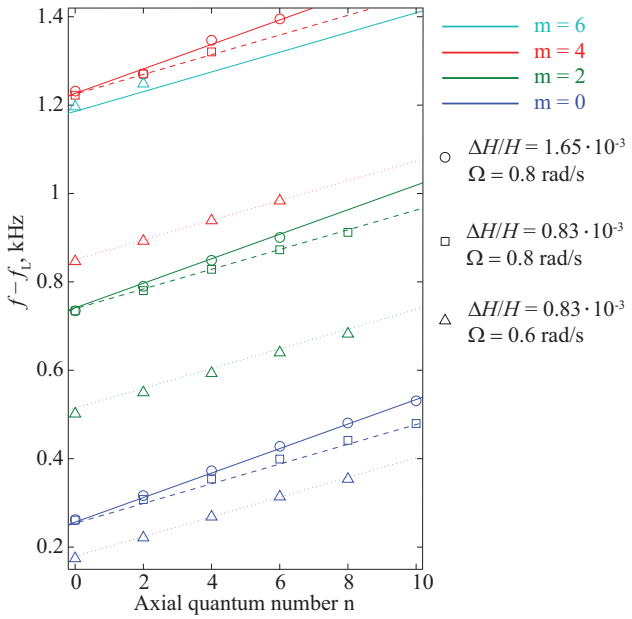

Figure 7.18: *The intersection points of the linear fits of spin-wave peak slopes and the frequency axis used for the determination of* ω_r *and* ω_z *shown in Fig. 7.17.*

7.4.3 Magnon-condensate in a magnetic trap

The way to measure the effect of rotation on the spin-wave peaks more carefully is to decrease the sweep range to a much smaller region, for instance, the region covering only the frequencies close to the Larmor frequency. In this way we can measure the shape and location of the few first spin-wave peaks more precisely. Additionally, we introduce a minimum into the NMR field H as seen in Fig. 7.16 [68]. The minimum is created by a small pinch coil (only 4 turns) around the top detector coil (Fig. 5.1). In this way we form an axial potential well, in addition to the radial potential well formed by the flare out texture. Thus we create a 3-dimensional harmonic potential trap where the magnetization precesses coherently and the spin-waves (or magnon excitations) form a condensate of quasiparticles.

Coherently precessing spin-waves in a trap have a spectrum determined by two quantum numbers, m and n:

$$\omega_{mn} = \omega_L + \omega_r(m+1) + \omega_z(n+1/2), \tag{7.7}$$

where ω_r and ω_z are radial and axial resonance frequencies, respectively. The rotation speed modifies the flare-out texture and the potential well as described in Sec. 7.3. This is seen as a change in ω_r: the higher the rotation speed the narrower the trap and the larger ω_r. Similarly, the depth of the minimum of H affects ω_z:

the deeper the trap the higher the resonance frequency. In our trap two series of excited levels are indeed experimentally observed. This is seen in Fig. 7.17 [68], where different peaks corresponding to different pairs of quantum numbers (m,n) are shown. Different spectra show the effect of changing the rotation speed Ω or the depth of the magnetic field, $\frac{\Delta H}{H}$. On the y-axis we have the ratio of magnetization, determined by the number of coherently precessing magnons inside the trap, to the magnetization measured in the Homogeneously Precessing Domain (HPD) mode, M_{HPD} [69]. The frequency sweep direction in the figure is from up to down, because for magnons $\frac{d\omega}{dN} < 0$, where N is the number of magnons in the trap. Thus, decreasing the frequency increases N, while Eq. (7.7) determines the frequency at which each excited state condensate starts to grow. A more detailed discussion about excited states of magnon condensates in a potential trap is found in Ref. [68].

The resonance frequencies ω_r and ω_z reported in Fig. 7.17 are determined by fitting straight lines to peak slopes and reading the intersections of the fits and the frequency axis. These points and the fits for the frequency determination are drawn in Fig. 7.18.

Chapter 8

Conclusions

In this thesis the new NMR setup of the ROTA cryostat is presented. Its working principles are similar to the system used before 2005, including the solenoidal pick-up coils and the cryogenic GaAs MESFET preamplifiers. However, the circuit layout and the preamplifier casing as well as the measurement frequencies are now different. During the years 2005 to 2007 measurements were performed with pick-up coils wound directly on the glass sample cylinder and with weak inductive coupling between the low-temperature resonator and the room temperature devices, instead of the cryogenic preamplifiers.

The present Q-factors are comparable to the ones measured in the old setup with preamplifiers before 2005. Compared to the setup without the preamplifiers we now have a better Q-factor in spectrometer A and worse in B. In our test setup we measured Q-factors as high as 40 000, but that is not possible in our actual measurement setup since the pick-up coils are so close to the surrounding NMR magnet system, introducing resistive RF losses in the RF shield. The present setup seems to provide less homogeneous polarization field distributions since the field inhomogeneity is now about twice as bad as it was before.

When it comes to comparing the signal to noise ratios between setups, we should notice that the whole cryostat was moved and rebuilt before installing the present NMR setup. During rebuilding some modifications were made to reduce heat leaks and vibrations and to improve the *SNR*, e.g., by changing the snap-on connectors to screwed ones and the flexible cables to semi-rigid ones, so the NMR circuitry itself is not the only change which has occurred. As a result, we measured $SNR_A = 5000$ and $SNR_B = 8000$ which are slightly better compared to the earlier values of 3000 and 7000 in the period 2005 – 2007.

By reintroducing the cryogenic preamplifiers we get better controllability of the NMR circuitry because of an adjustable coupling of the LC resonator to the room-temperature amplifier chain. This provides the possibility to adjust the Q-factor and the amplification of the low-temperature part of the circuit. Solenoidal

coils and cryogenic preamplifiers provide also easier handling and installing than a coil wound directly on quartz glass and a weak inductive coupling.

The line shape of the absorption signal measured in continuous wave NMR obeys the local oscillator model and depends on the axisymmetric flare-out-like textures in the sample cylinder. It depends strongly on temperature and rotation speed because of the textural orienting influence of the rotating counterflow. We performed many measurements in various conditions and were able to detect all the textures and peaks as defined by the texture theories. At present, our most important quantitatively measured feature from the signals is the height of the counterflow peak which is used to determine the number of vortices in the sample in various situations.

With spectrometer A we have an ideal opportunity to measure wide spin-wave spectra modifying the conventional spectrum predicted by the local oscillator model. The number of spin-wave resonance peaks is about 80, which is much more than detected in previous surveys because of lower temperatures. The spacing between adjacent peaks is found to change along the spectrum depending on temperature and rotation speed. We can improve spin-wave trapping by introducing a polarizing field minimum into the sample. As a result, the spin-waves are coherently precessing in a potential trap created by the flare-out texture and the magnetic field minimum. In the trap the spectrum of eigenstates can be changed by adjusting the rotation speed and the depth of the minimum of the magnetic field. These different excited states can be used to probe sensitively the order parameter texture at the lowest temperatures where conventional measuring signals become insensitive.

Overall, the present NMR approach works satisfactorily and is an improvement from the previous one (except for the field inhomogeneities). It gives us the possibility to measure the properties of the ^{3}He superfluids in the limit $T \to 0$, an important region with analogies to the vacuum properties of quantum matter in quantum field theories.

Bibliography

[1] F. Pobell, *Matter and Methods at Low Temperatures* (Springer-Verlag, 1992).

[2] A. M. Abdrakhimov, E. M. Galimov, and V. I. Vernadsky, *The Estimation of Helium-3 Probable Reserves in Lunar Regolith*, Lunar and Planetary Science XXXVIII (2007).

[3] H. H. Schmitt, *Return to the Moon* (Copernicus-Praxis, New York, 2006).

[4] R. Blaauwgeers, *Unconventional Quantized Vortices: A Study on ^3He and UPt_3*, Ph.D. thesis, Leiden University (2002).

[5] P. J. Hakonen, O. T. Ikkala, S. T. Islander, T. K. Markkula, P. M. Roubeau, K. M. Saloheimo, D. I. Garibashvili, and J. S. Tsakadze, *Rotating nuclear demagnetization refrigerator for experiments on superfluid ^3He*, Cryogenics **23**, 243 (1983).

[6] P. J. Hakonen, O. T. Ikkala, S. T. Islander, O. V. Lounasmaa, T. K. Markkula, P. Roubeau, K. M. Saloheimo, and G. E. Volovik, *NMR experiments on rotating superfluid ^3He-A: evidence for vorticity*, Physical Review Letters **48**, 1838 (1982).

[7] P. Hakonen, O. T. Ikkala, S. T. Islander, O. V. Lounasmaa, and G. E. Volovik, *NMR Experiments on Rotating Superfluid ^3He-A and ^3He-B and Their Theoretical Interpretation*, Journal of Low Temperature Physics **53**, 425 (1983).

[8] H. K. Seppälä, P. J. Hakonen, M. Krusius, T. Ohmi, M. M. Salomaa, J. T. Simola, and G. E. Volovik, *Continuous vortices with broken symmetry in rotating superfluid ^3He-A*, Physical Review Letters **52**, 1802 (1984).

[9] V. Ruutu, J. Koivuniemi, Ü. Parts, A. Hirai, and M. Krusius, *High sensitivity NMR measurements at low temperature and frequency*, Physica B **194-196**, 159 (1994).

[10] J. Koivuniemi and M. Krusius, *Cryogenic Amplifiers with Superconducting LC Resonator for Low Temperature NMR*, Report TKK-F-A777 (1998).

[11] Ü. Parts, J. H. Koivuniemi, M. Krusius, V. M. H. Ruutu, and S. R. Zakazov, *Nucleation of single vortex lines in rotating ^3He-B*, Physica B **194-196**, 771 (1994).

[12] Ü. Parts, V. M. H. Ruutu, J. H. Koivuniemi, Y. M. Bunkov, V. V. Dmitriev, M. Fogelström, M. Hubner, Y. Kondo, N. B. Kopnin, J. S. Korhonen, M. Krusius, O. V. Lounasmaa, P. I. Soininen, and G. E. Volovik, *Single-vortex nucleation in rotating ^{3}He-B*, Europhysics Letters **31**, 449 (1995).

[13] V. M. H. Ruutu, Ü. Parts, J. H. Koivuniemi, N. B. Kopnin, and M. Krusius, *Intrinsic and extrinsic mechanisms of vortex formation in superfluid ^{3}He-B*, Journal of Low Temperature Physics **107**, 93 (1997).

[14] A. J. Leggett, *A theoretical description of the new phases of liquid ^{3}He*, Reviews of Modern Physics **47**, 331 (1975).

[15] D. Vollhardt and P. Wölfle, *The Superfluid Phases of ^{3}He* (Taylor & Francis, London, 1990).

[16] G. E. Volovik, *Exotic Properties of Superfluid ^{3}He* (World Scientific, Singapore, 1992).

[17] M. M. Salomaa and G. E. Volovik, *Quantized vortices in supefluid ^{3}He*, Reviews of Modern Physics **59**, 533 (1987).

[18] O. V. Lounasmaa and E. Thuneberg, *Vortices in rotating superfluid ^{3}He*, Proceedings of the National Academy of Sciences of the United States of America **96**, 7760 (1999).

[19] V. P. Mineyev and G. E. Volovik, *Planar and linear solitons in superfluid ^{3}He*, Physical Review B **18**, 3197 (1978).

[20] D. R. Tilley and J. Tilley, *Superfluidity and Superconductivity* (Adam Hilger, Bristol, 1990).

[21] P. W. Anderson and W. F. Brinkman, *Anisotropic Superfluidity in ^{3}He: A Possible Interpretation of Its Stability as a Spin-Fluctuation Effect*, Physical Review Letters **30**, 1108 (1973).

[22] R. Balian and N. R. Werthamer, *Superconductivity with Pairs in a Relative p Wave*, Physical Review **131**, 1553 (1963).

[23] E. M. Lifshitz and L. P. Pitaevskii, *Statistical Physics, Part 2, Landau and Lifshitz Course of Theoretical Physics* (Butterworth-Heinemann, 1980).

[24] E. R. Dobbs, *Helium Three* (Oxford University Press, 2000).

[25] C. F. Barenghi, R. J. Donnelly, and W. F. Vinen, *Friction on Quantized Vortices in Helium II. A Review*, Journal of Low Temperature Physics **52**, 189 (1983).

[26] E. V. Thuneberg, *Identification of Vortices in Superfluid ^{3}He-B*, Physical Review Letters **56**, 359 (1986).

[27] Y. Kondo, J. S. Korhonen, M. Krusius, V. V. Dmitriev, E. V. Thuneberg, and G. E. Volovik, *Combined Spin-Mass Vortex with Soliton Tail in Superfluid ^{3}He-B*, Physical Review Letters **68**, 3331 (1992).

[28] C. P. Slichter, *Principles of Magnetic Resonance*, *Springer Series in Solid State Sciences*, vol. 1 (Springer-Verlag, Berlin, 1978).

[29] J. P. Hornak, *The Basics of NMR*, Rochester Institute of Technology, http://www.cis.rit.edu/htbooks/nmr/bnmr.htm (1997).

[30] S. Arvela, *Resonance Circuit in NMR Measurements*, *Special Assignment*, Helsinki University of Technology (2001).

[31] P. Heikkinen, *High-Q LC resonance circuit as input to a GaAs MESFET preamplifier at LHe temperatures*, *Special Assignment*, Helsinki University of Technology (2009).

[32] M. Bonaldi, P. Falferi, R. Dolesi, M. Cerdonio, and S. Vitale, *High Q tunable LC resonator operating at cryogenic temperature*, Review of Scientific Instruments **69**, 3690 (1998).

[33] A. J. Leggett, *The spin dynamics of an anisotropic fermi superfluid (^{3}He?)*, Annals of Physics **85**, 11 (1974).

[34] H. Smith, W. F. Brinkman, and S. Engelsberg, *Textures and NMR in superfluid ^{3}He-(B)*, Physical Review B **15**, 199 (1977).

[35] W. F. Brinkman and M. C. Cross, *Spin and Orbital Dynamics of Superfluid ^{3}He*, Progress in Low Temperature Physics **VIIA**, 105 (1978).

[36] E. V. Thuneberg, *Hydrostatic Theory of Superfluid ^{3}He-B*, Journal of Low Temperature Physics **122**, 657 (2001).

[37] E. V. Thuneberg, *Surfaces of Superfluid ^{3}He-B*, Physical Review B **33**, 5124 (1986).

[38] A. D. Gongadze, G. E. Gurgenishvili, E. V. Thuneberg, and G. A. Kharadze, Fizika Nizkikh Temperatur **7**, 821 (1981).

[39] J. W. Serene and D. Rainer, *The quasiclassical approach to superfluid ^{3}He*, Physics Reports **101**, 221 (1983).

[40] J. Kopu, R. Schanen, R. Blaauwgeers, V. B. Eltsov, M. Krusius, J. J. Ruohio, and E. V. Thuneberg, *NMR Line Shape of Rotating ^{3}He-B at Large Counterflow Velocity*, Journal of Low Temperature Physics **120**, 213 (2000).

[41] A. J. Leggett and S. Takagi, *Orientational dynamics of superfluid ^{3}He: A "two-fluid" model. l. Spin dynamics with relaxation*, Annals of Physics **106**, 79 (1977).

[42] J. S. Korhonen, A. D. Gongadze, Z. Janú, Y. Kondo, M. Krusius, Y. M. Mukharsky, and E. V. Thuneberg, *Order-Parameter Textures and Boundary Conditions in Rotating Vortex-Free ^{3}He-B*, Physical Review Letters **65**, 1211 (1990).

[43] A. I. Ahonen, M. Krusius, and M. A. Paalanen, *NMR Experiments on the Superfluid Phases of ^{3}He in Restricted Geometries*, Journal of Low Temperature Physics **25**, 421 (1976).

[44] D. S. Greywall and P. A. Busch, *^{3}He-Melting-Curve Thermometry*, Journal of Low Temperature Physics **46**, 451 (1982).

[45] R. K. Kirschman, Proceedings from Low Temperature Electronics and High Temperature Superconductivity **93-22**, 223 (1993).

[46] R. K. Kirschman and J. A. Lipa, Proceedings from Conference on Infrared Detectors and Instrumentation SPIE **1946**, 350 (1993).

[47] *Roch Schanen's material (in paper form) on the old preamplifier circuit board and on the bias voltage source can be found in a green folder at the ROTA cryostat.*

[48] T. L. Floyd, *Electronic Devices* (Prentice Hall, 2002), 6th edn.

[49] P. Horowitz and W. Hill, *The Art of Electronics* (Cambridge University Press, 1989), 2nd edn.

[50] *Eliminating Parasitic Oscillation between Parallel MOSFETs*, *Tech. Rep.*, Advanced Power Technology (2004).

[51] K. Silvonen, *Sähkötekniikka ja elektroniikka* (Otatieto, 2003).

[52] M. Blaẑková, M. Ĉloveĉko, V. B. Eltsov, R. de Graaf, J. J. Hosio, M. Krusius, D. Schmoranzer, W. Schoepe, L. Skrbek, P. Skyba, R. E. Solntsev, and W. F. Vinen, *Vibrating Quartz Fork - a Tool for Cryogenic Helium Research*, Journal of Low Temperature Physics **150**, 525 (2008).

[53] A. P. Finne, S. Boldarev, V. B. Eltsov, and M. Krusius, *Vortex Formation in Neutron-Irradiated Rotating Superfluid ^{3}He-B*, Journal of Low Temperature Physics **135**, 479 (2004).

[54] G. Vandegrift, *Deducing the width of a Lorentzian resonance curve from experimental data*, American Journal of Physics **61**, 473 (1993).

[55] J. B. Wooten, J. Jacobus, J. E. Gurst, W. Egan, W. G. Rhodes, and K. Wagener, *Nuclear Spin-Lattice Relaxation Times from Continuous Wave NMR Spectroscopy*, Journal of Chemical Education **56**, 304 (1979).

[56] P. C. Hammel and R. C. Richardson, *Relaxation of Nuclear Magnetization of Liquid ^{3}He in Confined Geometries*, Physical Review Letters **52**, 1441 (1984).

[57] L. J. Friedman, T. J. Gramila, and R. C. Richardson, *Magnetic Coupling of ^{3}He with a Fluorocarbon Substrate*, Journal of Low Temperature Physics **55**, 83 (1984).

[58] S. Maegawa, A. Schuhl, M. W. Meisel, and M. Chapellier, *Frequency and Temperature Dependence of the Relaxation Times of Liquid ^{3}He Confined by Fluorocarbon Microspheres*, Europhysics Letters **1**, 83 (1986).

[59] A. Schuhl, S. Maegawa, M. W. Meisel, and M. Chapellier, *Production of Enhanced Liquid ^{3}He Magnetization by Dynamic Nuclear Polarization*, Physical Review Letters **54**, 1952 (1985).

[60] N. Alikacem, D. T. Sprague, and R. B. Hallock, *Energetics of ^{3}He States in ^{4}He Films*, Physical Review Letters **67**, 2501 (1991).

[61] R. L. Garwin and H. A. Reich, *Self-Diffusion and Nuclear Relaxation in ^{3}He*, Physical Review **115**, 1478 (1959).

[62] G. Careri, I. Modena, and M. Santini, *Spin-Lattice Relaxation Time in Liquid ^{3}He*, Il Nuovo Cimento **13**, 207 (1959).

[63] N. Bloembergen, E. M. Purcell, and R. V. Pound, *Relaxation Effects in Nuclear Magnetic Resonance Absorption*, Physical Review **73**, 679 (1948).

[64] R. de Graaf, V. B. Eltsov, J. J. Hosio, P. Heikkinen, R. Hänninen, and M. Krusius, *Order Parameter Textures of Superfluid ^{3}He in Applied Flow and Quantitative Comparison with Hydrostatic Theory*, Poster in Symposia on Superfluids under Rotation (2010).

[65] V. B. Eltsov, R. de Graaf, P. J. Heikkinen, J. J. Hosio, R. Hänninen, M. Krusius, and V. S. L'vov, *Super Stability of Laminar Vortex Flow in Superfluid ^{3}He-B*, arXiv:1005.0546 [cond-mat.other] (2010).

[66] D. D. Osheroff, Physica B **90**, 20 (1977).

[67] P. J. Hakonen, M. Krusius, M. M. Salomaa, R. H. Salmelin, J. T. Simola, A. D. Gongadze, G. E. Vachnadze, and G. A. Kharadze, *NMR and Axial Magnetic Field Textures in Stationary and Rotating Superfluid ^{3}He-B*, Journal of Low Temperature Physics **76**, 225 (1989).

[68] Y. M. Bunkov, V. B. Eltsov, R. de Graaf, P. J. Heikkinen, J. J. Hosio, M. Krusius, and G. E. Volovik, *Non-ground-state Bose-Einstein condensates of magnons in superfluid ^{3}He-B*, arXiv:1002.1674v1 [cond-mat.quant-gas] (2010).

[69] G. E. Volovik, *Twenty Years of Magnon Bose Condensation and Spin Current Superfluidity in ^{3}He-B*, Journal of Low Temperature Physics **153**, 266 (2008).